OPEN ACCESS
IOP Publishing
Smart Materials and Structures
Smart Mater. Struct. **34** (2025) 025049 (20pp)
https://doi.org/10.1088/1361-665X/adad21

Parametric design studies of GATOR morphing fairings for folding wingtip joints

Nuhaadh Mohamed Mahid*, Mark Schenk, Branislav Titurus and Benjamin King Sutton Woods

School of Civil, Aerospace and Design Engineering, University of Bristol, Bristol, BS8 1TR, United Kingdom

E-mail: nuhaadh.mahid@bristol.ac.uk, m.schenk@bristol.ac.uk, Brano.Titurus@bristol.ac.uk and ben.k.s.woods@bristol.ac.uk

Received 25 September 2024, revised 28 November 2024
Accepted for publication 22 January 2025
Published 31 January 2025

Abstract

This paper presents the modelling of a morphing fairing designed to cover the joint on hinged commercial airliner wingtips, such as the semi-aeroelastic Hinge concept. The fairing is made from geometrically anisotropic thermoplastic rubber morphing skin panels, which are 3D-printed multi-material thermoplastic polyurethane sandwich panels combining flexible facesheets with zero Poisson's ratio cellular cores to provide large extension capability alongside high out-of-plane stiffness. The morphing fairing is designed to cover the gaps in the hinge with a smooth and continuous surface while minimising added torsional stiffness and distortion of the aerofoil cross-section during wingtip rotation. In order to model the mechanical response of this structure at a reasonable computational cost, a homogenisation approach is proposed, wherein the elastic properties of the panel are homogenised to an equivalent shell stiffness matrix through detailed finite element studies on unit cells. These equivalent shell properties are then applied to the three-dimensional geometry of the wing to predict the global response of the fairing during wingtip rotation. This model is then used to parametrically study the effects of varying panel and fairing design parameters on the two design objectives of minimising torsional stiffness and cross-section distortion. The study indicates that cross-section distortion is best minimised by increasing the skin panel's core thickness, with the other panel design variables having significantly less impact. In contrast, all design variables significantly affect torsional stiffness, with decreasing facesheet thickness and increasing core chevron wall length and chevron angle being particularly effective at reducing torque. The impact of pre-straining the skin panels is also studied, as is the use of additional internal ribs within the fairing, where both approaches reduce distortion at the cost of modestly higher torque. Together, these results clearly indicate the underlying design trends, useful ranges of design variables, and the strong competition between design objectives.

Keywords: adaptive structures, folding wingtip, morphing aircraft, multi-scale modelling

* Author to whom any correspondence should be addressed.

1. Introduction

Commercial aircraft spend most of their flight time in the cruise phase, where induced drag is still a major component of total drag. High aspect ratio wing configurations are pursued to reduce the induced drag and thereby reduce fuel consumption. Designing wings with longer spans is a simple way to achieve a higher aspect ratio; however, airport gates limit the wingspan in commercial aircraft according to the categories shown in table 1.

A foldable wingtip circumvents this restriction by folding it after landing to fit within the airport gate size and unfolding it before taking off to extend the wingspan. This approach is used by the Boeing 777X, which has a 71.75 m wingspan in flight with extended wingtips and a 64.85 m wingspan at the gate with folded wingtips [3]. Hence, the folded wingtip enables gate compatibility to ICAO Code E and FAA Group V, although the wingspan in flight is longer than the compatible limit [1, 2]. Moreover, airports charge higher fees for larger gates and tend to have restricted numbers of them, so folding wingtips can save the airlines significant recurring costs.

Despite the aerodynamic benefits, wingspan extension increases bending moments at the wing root due to the extended moment arm. The extended moment arm is particularly problematic for the peak gust loads that are a key driver in structural sizing and, therefore, wing weight. The folding wingtip can be designed to provide gust load alleviation if it is allowed to rotate freely during flight with its axis of rotation oriented at an angle outward from the direction of flight [4, 5]. The flight tests show that this free folding response of the flared wingtip is statically and dynamically stable throughout the flight [6]. The 'flaring' of the hinge by a flare angle (Λ) relative to the aircraft's longitudinal axis, shown schematically in figure 1, is a key component of the semi-aeroelastic hinge (SAH) concept currently under development by Airbus, the University of Bristol, and others [7].

The flare angle introduces a geometric coupling between the folding angle (θ) and the local angle of airflow incidence on the wingtip. For positive flare angles, as the wingtip folds up, the angle of incidence on the wingtip is reduced in a way which tends to reduce lift during a gust. Aeroelastic studies have shown that this gust rejection capability, combined with reductions in root bending moment stemming from the lack of moments carried across the hinge, can allow for a significant 25% increase in the wingspan with only a minimal 4.4% increase in peak loads [9]. Hence, it enables wingspan extension while retaining gate width compatibility and with minimal additional structural reinforcement.

The SAH joint requires a fairing to enclose the gap between the inner and outer wing and provide as smooth an aerodynamic surface as possible. Moreover, the SAH concept may include further mechanical components (e.g. actuators) within the joint itself that may require increased internal volume and thickness, thereby protruding the fairing into the flow. One solution to designing this fairing would be to take a purely mechanical approach, with discrete sliding interfaces carefully designed to minimise gaps in the surface but with an associated increase in mechanical complexity and maintenance requirements. However, the complex three-dimensional geometry of the fairing and the misalignment of the sliding interfaces to the flow due to the flare angle make it difficult to avoid surface discontinuities at large wingtip rotations. These discontinuities on the aerodynamic surface can lead to significant drag penalties and difficulties in sealing the internal components, both aerodynamically and in terms of water/debris ingress.

Table 1. Wingspan restrictions for airport gate compatibility [1, 2].

ICAO Code	FAA Group	Wingspan
A	I	$<$15 m
B	II	15—24 m
C	III	24—36 m
D	IV	36—52 m
E	V	52—65 m
F	VI	65—80 m

Alternatively, a compliance-based morphing approach could be taken, using geometrical and material compliance to create an intrinsically smooth and gapless surface which deforms compliantly during wingtip rotation. The geometry of this surface could be freely optimised due to the removal of constraints around mechanical interfaces needing to be radially symmetrical, allowing for the flare angle to be more effectively 'hidden' from the flow. The authors previously introduced the concept investigated here for achieving a morphing SAH fairing based on compliant skins supported by pivoting ribs [10]. In this concept, which is shown in figure 2, the inboard wing and outboard wingtip spars connect to the hinge joint, and a central rib pivoting around the hinge supports the fairing.

The pivoting rib shares the same axis of rotation with the wingtip joint and is able to rotate freely (separately from wing joint rotation) to balance the moments created by the upper and lower compliant skins in a way that helps balance the required deformations on either side of the rib, thereby reducing both the peak strain on the fairing and the folding stiffness of the joint [10]. The pivoting rib also has the benefit of enforcing the separation between the joint and the skins, avoiding any contact or interference between them as the wingtip folds. Additionally, the present study introduces floating ribs, which are only connected to the skin panels. These floating ribs connect the top and bottom skin, periodically enforcing the aerofoil cross-section shape in their locations. They also shorten the unsupported spanwise length of the panels, thereby reducing their out-of-plane deformation. The implementation and efficacy of this new addition to the overall concept is one of the aspects studied in this work.

The fairing skins are proposed to be sandwich panels made from a zero Poisson's ratio core and elastomeric facesheets. The zero Poisson's ratio decouples the deformation in the morphing direction from the direction perpendicular to it. This decoupling enables large deformations in the morphing direction without significant necking effects. Corrugated sheets [12, 13] and cellular cores [14, 15] have previously been proposed

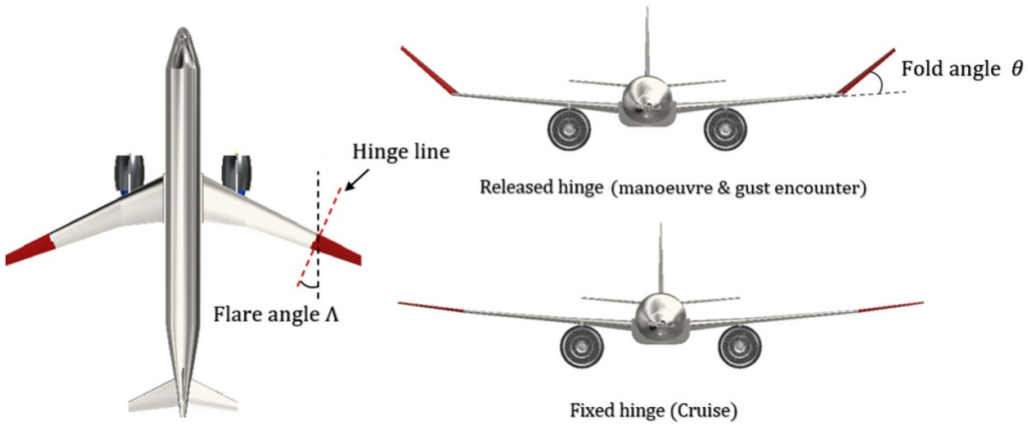

Figure 1. Semi-aeroelastic hinge (SAH) concept. Reproduced from [8]. CC BY 4.0.

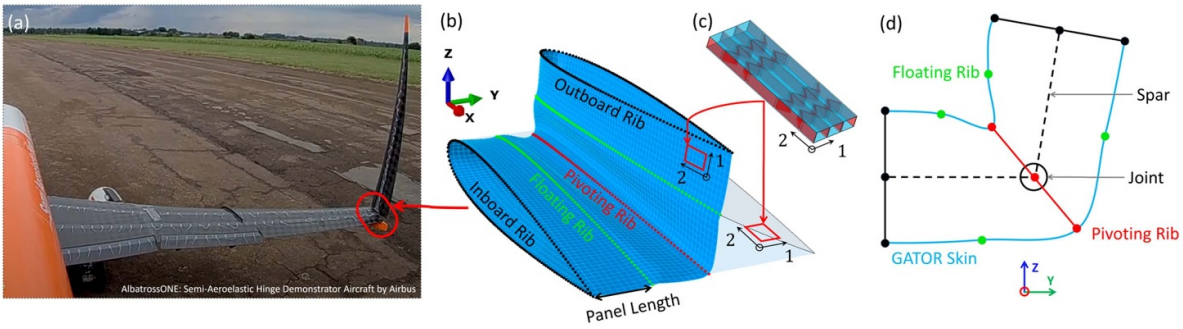

Figure 2. GATOR panel fairing proposed for folding wingtip joints. (a) Shows the location of the proposed fairing on AlbatrossONE, a small-scale flying demonstrator of the SAH concept. Reproduced with permission from [11]. © Airbus. (b) Shows the fairing section with its supporting ribs. The fairing section is modelled as a shell surface with homogenised properties of the GATOR panel. (c) Shows the GATOR sandwich panel. (d) Shows the rear view (*YZ*-plane) of the fairing with the connectivity of the supporting ribs.

as zero Poisson's ratio cores for camber morphing [12], span extension [14, 15] and folding wingtip [13] fairings. Cellular cores are pursued in this work over the corrugated sheets due to their higher achievable axial deformations and greater design freedom in tailoring the equivalent elastic properties of the core. While different unit cell shapes can produce a zero Poisson's ratio cellular core, this work considers cores made from parallel ribs connected via bending chevrons [16] (known specifically as MorphCore and more generally as an 'accordion' geometry), as shown in figure 2(c). This core geometry is preferred due to its simplicity and higher out-of-plane stiffness relative to other zero Poisson's ratio cores [17]. Facesheets are attached to the top and bottom of this core to make a sandwich panel which provides a continuous outer surface for airflow. The separation distance between the two facesheets created by the core provides the out-of-plane rigidity to carry the aerodynamic pressure loads. This sandwich panel can be manufactured via the fused filament fabrication 3D printing technique, as demonstrated by previous work on the geometrically anisotropic thermoplastic rubber (GATOR) morphing skin concept [18, 19].

Due to the presence of many small features, sandwich panels with cellular cores require a fine mesh to achieve converged finite element (FE) analysis results. Hence, they are computationally expensive to model in large structures such as a wing section, where there could easily be thousands of unit cells. An alternative is a two-scale approach, as indicated in figure 2, where a homogenisation process determines the equivalent shell properties of the sandwich panel, and a shell surface is used to model the sandwich panel on the wing section [20]. The latter can be implemented in commercial FE solvers (e.g., Abaqus) by defining the elastic properties of the shell elements using an equivalent shell stiffness matrix. This equivalent shell stiffness matrix can be found by either an analytical [17] or FE-based [21, 22] homogenisation process on a unit cell of the sandwich panel. The FE-based homogenisation approach is pursued in this study as it captures the effects of chevron-facesheet interaction [23], which is not captured in the analytical approach based on the classical laminate theory [20]. The two-scale modelling approach significantly reduces the computational cost relative to a full-scale simulation of the fairing deformation, enabling a parametric study of the design space.

This paper uses the two-scale modelling approach to study the effects of the GATOR panel geometry and other fairing variables on the torsional stiffness and the cross-section distortion of the fairing [20]. First, the equivalent elastic properties of the GATOR panel are found using an FE-based homogenisation on a unit cell [21], which is the smallest repeating unit shown in figure 2(c). Then, a shell fairing with

the homogenised properties of the GATOR panel is used to simulate the deformation of the fairing as the wingtip folds. The study aims to reduce the torsional stiffness and the distortion of the fairing as the wingtip folds by tuning the GATOR panel and the fairing variables. Hence, this paper presents a parametric study of the design space offered by the GATOR panels as a fairing for folding wingtip joints.

The following section of the paper presents the methods used for homogenising the sandwich panels and generating the fairing models, along with the definition of the metrics used to measure the objectives. The subsequent section presents the results from the analysis, along with a discussion of the findings. The results are presented for a sensitivity study identifying the variables strongly affecting the objectives and a parametric study identifying trends of the objectives with the design variables. Finally, the conclusions highlight the insights from the study and their significance for further analysis of the concept.

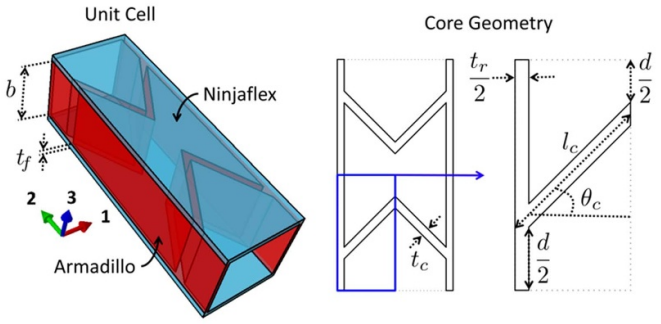

Figure 3. The geometry of the GATOR panel unit cell.

Table 2. Elastic properties of the materials used for the panel [18].

Property		Armadillo	Ninjaflex
Young's Modulus	[MPa]	396	22.9
Poisson's ratio		0.48	0.48

2. Modelling

The homogenisation of the unit cell's elastic response captures the equivalent shell stiffness of the plate at specific deformation states. These deformation states can be represented as shell strain states consisting of in-plane strains and out-of-plane curvatures. The equivalent shell stiffness evaluated at a given strain state may change significantly as the plate deforms further due to geometric nonlinearity in the deformation and the nonlinearity in the materials' response [23]. The geometric nonlinearity in deformation can be captured by homogenising the unit cell at each strain state and updating the shell stiffness matrix of each shell element in the fairing based on their strain state during the simulation (e.g., the FE^2 method [22]). However, this approach is more expensive than running a full-scale simulation, as a unit cell model is spawned for each integration point of shell elements in the fairing and homogenised simultaneously with the fairing simulation [22]. An alternative approach is to pre-compute a database of equivalent shell stiffness matrices at various strain states and update the shell element's constitutive properties using interpolated values from the database. While this approach is computationally cheaper than the FE^2 method, it still requires extensive pre-computation of all achievable strain states for every unit cell geometry. Given this, a simpler approach assuming linear elastic stiffness properties is preferred for this initial parametric study to reduce the computational cost further. The linear elastic stiffness properties from the undeformed GATOR panel are used in the shell model. Hence, the changes in the stiffness of the GATOR panel due to geometrically nonlinear deformation are not accounted for in the shell model used in this study. The effect of assuming linear elastic stiffness to reduce computational cost is studied in section 2.3 by comparing the shell model with a full-scale model for a simplified model representative of a fairing slice along the span at the thickest aerofoil location.

The GATOR panels manufactured in previous work were fabricated via muti-material 3D printing using two different formulations of thermoplastic polyurethane manufactured by Ninjatek. A soft material, 'Ninjaflex', capable of 65% strain before yield [24], is used for the facesheets, while a stiffer material, 'Armadillo', capable of 18% strain before yield [25], is used for the core, as shown in figure 3.

The experimental tests on the GATOR panels show noticeable material-induced softening at high strain states and hysteresis response in cyclic loading [18]. Hence, a hyper-elastic material model should ideally be used in homogenising panel stiffness to capture the complex material response across the whole elastic deformation range. However, for strains less than 10%, the experimental results show good agreement with FE simulation using linear elastic mechanical properties for Ninjaflex and Armadillo [18]. As the current study evaluates the GATOR panel's initial stiffness response, the same linear elastic material properties from the literature [18] are used in this homogenisation process. These material properties are shown in table 2.

The unit cell's geometry significantly affects the panel's equivalent stiffness properties. The homogenisation process evaluates an equivalent shell stiffness matrix at the panel's undeformed strain state. This shell stiffness matrix is used as linear elastic constitutive properties for the shell model of the fairing section shown in figure 2(b). The desired properties of the shell stiffness to achieve low torsional stiffness and distortion of the fairing include high in-plane flexibility in the morphing direction (i.e., 1-axis), near-zero Poisson's ratio in the non-morphing direction (i.e., 2-axis), and high out-of-plane stiffness. The effects of unit cell geometry on these properties are studied using the range of values and default configuration shown in table 3.

The range of values used for each panel variable is adapted from the previous parametric study of the GATOR panel [23] to capture the geometry with the desired properties for the fairing. The default configuration is arbitrary and approximately represents the mid values of the ranges.

Table 3. Variables of the sandwich panel.

Variable		Default	Minimum	Maximum	Unit
Chevron angle	θ_c	60.0	40.0	70.0	deg
Chevron wall length	l_c	12.5	5.0	20.0	mm
Chevron wall thickness	t_c	1.0	0.5	1.5	mm
Chevron separation	d	6.0	2.0	10.0	mm
Rib thickness	t_r	1.0	0.5	1.5	mm
Core thickness	b	11.0	2.0	20.0	mm
Facesheet thickness	t_f	0.8	0.1	1.5	mm

Table 4. Variables of the fairing section.

Variable		Default	Minimum	Maximum	Unit
Pre-tension	ε_p	0.1	0	0.2	
Span	L	0.8	0.6	1.0	m
Floating ribs	n_{fr}	0	0	2	

The fairing section has a root chord (c) of 1.6 m, representing the tip chord of a typical single-aisle commercial jet airliner (e.g., A320 aircraft [26]). A symmetric aerofoil profile, in this case, NACA 0015, is used to avoid folding deformation of the wingtip due to applied pre-tension on the skin panels. In an unsymmetric aerofoil profile, the unbalanced moment contribution from the top and bottom skins due to pre-tension will result in a non-zero initial folding angle. While this is not expected to cause any real issue during the implementation of the device (it would just cause small offsets in the torque response curves), for this parametric study, it is helpful to have the partial simplification of a symmetric initial condition. Additionally, the wing section used for the analysis has no taper, sweep or flare angle, further simplifying the fairing geometry. This model is used to study the effects of varying fairing variables on the objectives of low torsional stiffness and cross-section distortion. The default configuration and the range of values for the fairing variables are shown in table 4.

The range of values used for each fairing variable is adapted from the previous parametric study of the fairing for folding wing joints [10]. The default configuration represents the mid values of the ranges, except for the floating ribs whose default value is zero, as they are newly introduced in this study.

The stiffness matrix required to define the constitutive properties of shell elements depends on the shell formulation used in the fairing section. A shell surface modelled using the Kirchoff–Love plate theory only requires the in-plane stiffness matrix (**A**), out-of-plane stiffness matrix (**D**) and the coupling matrix between the in-plane and the out-of-plane deformation (**B**) to define its constitutive properties. The formulation assumes that the plate's thickness remains unchanged and the cross-section remains straight and perpendicular to the mid-plane after deformation. These assumptions are valid for panels with negligible transverse shear flexibility. The effect of transverse shear flexibility is negligible for panels with a high length-to-thickness ratio (typically $\geqslant$15 for homogenous plates [27]).

The homogenisation process uses a unit cell of the GATOR panel as the representative volume element (RVE). In the default configuration, this unit cell has the dimensions 12.5 $\times$ 35.9 $\times$ 12.6 mm in 1, 2, and 3 directions, respectively. For simplicity, these dimensions are referred to as the length, width and thickness, respectively. In the default configuration with no floating ribs, the length-to-thickness ratio is 31.7 for the unsupported panel length between ribs. Given the high length-to-thickness ratio in the default configuration, the Kirchoff–Love plate theory is used to simulate the panel deformation, thereby ignoring the effects of transverse shear deformation. However, it is noted that the length-to-thickness ratio of the panel changes with the panel thickness, the fairing span and the number of floating ribs. For the thickest panel, the shortest span and the most floating ribs, the length-to-thickness ratios of the panel are 17.4, 23.8 and 10.6, respectively. Hence, in all but one case, the length-to-thickness ratio of the panel exceeds the typical value of 15 used as a threshold for homogenous plates [27]. Additionally, for accurate results with a two-scale modelling approach, the length scale of the RVE should be at least an order of magnitude smaller than the panel length scale [28]. In this case, the shortest panel length configuration (i.e., fairing with 2 floating ribs) gives a panel length to RVE length ratio of 10.7 in the morphing direction (i.e., 1-axis), providing sufficient scale separation to use the two-scale modelling approach.

The simplifications described above enable a computationally affordable design space exploration of the fairing via a two-scale modelling approach. In exchange, the use of linear material properties in the RVE and linear homogenised stiffness properties in the fairing may not provide accurate results for large folding angles of the wingtip. However, the two-scale approach provides adequate fidelity to study the effects of the design variables on the fairing objectives in low folding angles. The fairing designs with high torsional stiffness and large distortions at low folding angles are not viable for large folding angles of the wingtip, and the proposed modelling approach can identify these designs, thereby reducing the design space to feasible solutions. Hence, the two-scale modelling approach is useful for understanding the basic design trade-offs and highlighting promising configurations for future analysis with more expensive methods better suited to capturing material and geometric nonlinearity.

2.1. Homogenisation of the flexible sandwich panel

Various forms of homogenisation for cellular cores and sandwich panels have been explored in literature. Analytical approaches to homogenisation typically use equivalent core properties and isotropic facesheet properties with the classical laminate theory to evaluate the shell stiffness matrix for the sandwich panel. The equivalent properties of the core are evaluated by modelling the deformation of the cell walls as shear deformable beams [14, 17, 29, 30]. The equivalent properties evaluated using this approach for an isolated core with thin walls have shown good agreement with FE simulation results [30]. However, in a sandwich panel, the intermittent bonding between the core and flexible facesheets introduces non-uniform deformations on the facesheets [23]. The classical laminate theory does not capture these effects; hence, the

analytical homogenisation underpredicts the stiffness of the sandwich panel.

FE-based homogenisation approaches model a RVE with periodic boundary conditions (PBC). The RVE is deformed in each shell deformation mode to evaluate the corresponding column of the shell stiffness matrix [21]. FE-based homogenisation offers a robust method of homogenising a wide range of unit cells by giving the flexibility to use beam, shell or solid elements depending on the wall dimensions of the core. For instance, the cell walls in thick cores have low aspect ratios, which deviate from beam theory assumptions. These walls must be modelled using either shell or solid elements. Similarly, in cases where the cell walls are thick, they must be modelled with solid elements. Moreover, FE-based homogenisation can capture the effects of non-uniform deformation on the facesheets. Hence, this approach is more suitable for homogenising the elastic properties of the flexible sandwich panels studied here than the analytical approach described above.

The unit cell of the panel is modelled using linear elastic material properties and homogenised using linear perturbation from the undeformed state. The unit cell, shown in figure 3, is the RVE that tessellates to form a continuous panel. Hence, the deformation on each side of the unit cell must be compatible with the corresponding deformation of the side of the adjacent unit cells. This constraint is enforced by the PBCs, which are applied as equations coupling the deformation of a pair of nodes on opposite faces of the RVE. The PBCs for a plate constitute in-plane and out-of-plane equations applied only on nodes at the vertical faces, as the top and bottom faces remain traction-free [21].

Consider an RVE symmetric about all three axes and centred at the origin. Let $x^{\text{face}}_{\text{DOF}}$ and $u^{\text{face}}_{\text{DOF}}$ be the coordinates and displacements of the nodes, where the superscript refers to faces in each axis (e.g., 1 for the positive face and 2 for the negative face of the axis), and the subscript refers to the degree of freedom of the node. The constraint equations linking the pair of nodes on opposite vertical faces are shown in Equation 1, followed by the definition of their coefficients [21, 31, 32],

$$\begin{bmatrix} u^1_1 \\ u^1_2 \\ u^1_3 \end{bmatrix} - \begin{bmatrix} u^2_1 \\ u^2_2 \\ u^2_3 \end{bmatrix} = \begin{bmatrix} \Delta x_1 & 0 & \frac{1}{2}\Delta x_2 & z\Delta x_1 & 0 & \frac{1}{2}z\Delta x_2 \\ 0 & \Delta x_2 & \frac{1}{2}\Delta x_1 & 0 & z\Delta x_2 & \frac{1}{2}z\Delta x_1 \\ 0 & 0 & 0 & 0 & 0 & \frac{1}{2}C \end{bmatrix} \times \begin{bmatrix} \varepsilon_{11} \\ \varepsilon_{22} \\ \gamma_{12} \\ \kappa_{11} \\ \kappa_{22} \\ \kappa_{12} \end{bmatrix} \tag{1}$$

where:

$$\Delta x_1 = x^1_1 - x^2_1, \quad \Delta x_2 = x^1_2 - x^2_2,$$

$$z = x^1_3 = x^2_3, \quad C = -\left(x^1_1 x^1_2 - x^2_1 x^2_2\right).$$

Additional reference nodes, n^{ε} and n^{κ} are introduced to the FE model to apply RVE deformation using the displacement of the reference nodes. The locations of these reference nodes are arbitrary; hence, they are not specified here, as only their displacements affect the RVE deformation. The in-plane deformation of the RVE due to strains ε_{11}, ε_{22} and γ_{12} are applied via the displacement of the reference node n^{ε} in degrees of freedom 1, 2 and 3, respectively. Similarly, the out-of-plane deformation of the RVE due to curvatures κ_{11}, κ_{22} and κ_{12} are applied via the displacement of the reference node n^{κ}. Note that the shear strain (γ_{12}) and torsional curvature (κ_{12}) are defined in the engineering form (i.e., $\gamma_{12} = \frac{\partial u_1}{\partial x_2} + \frac{\partial u_2}{\partial x_1}$ and $\kappa_{12} = \frac{2\left(\partial^2 u_3\right)}{\partial x_2 \partial x_1}$); hence, a factor of $\frac{1}{2}$ is used with the coefficient of these deformation modes.

To populate the stiffness matrix, the unit cell is deformed in each shell deformation mode while keeping the deformations in the other modes zero. For instance, an axial strain $\varepsilon_{11} = 1$ is applied via displacements on reference nodes $u^{\varepsilon}_1 = 1$ and $u^{\varepsilon}_2 = u^{\varepsilon}_3 = u^{\kappa}_1 = u^{\kappa}_2 = u^{\kappa}_3 = 0$. The reaction loads are extracted from the reference nodes and divided by the unit cell's initial in-plane area to evaluate the column of the shell stiffness matrix $\boldsymbol{K}_{\text{plate}}$ corresponding to the applied deformation. The expression for the shell stiffness matrix is shown in equation (2),

$$\boldsymbol{K}_{\text{plate}}(:, i) = \frac{1}{u_i A_{\text{RVE}}} \boldsymbol{F} \tag{2}$$

where:

$$\boldsymbol{K}_{\text{plate}} = \begin{bmatrix} \mathbf{A} & \mathbf{B} \\ \mathbf{B} & \mathbf{D} \end{bmatrix},$$

$$\boldsymbol{F} = [F^{\varepsilon}_1, F^{\varepsilon}_2, F^{\varepsilon}_3, F^{\kappa}_1, F^{\kappa}_2, F^{\kappa}_3]^{\mathrm{T}},$$

$$\boldsymbol{u} = [u^{\varepsilon}_1, u^{\varepsilon}_2, u^{\varepsilon}_3, u^{\kappa}_1, u^{\kappa}_2, u^{\kappa}_3]^{\mathrm{T}}.$$

The variable A_{RVE} is the in-plane area of the RVE (i.e. 1–2 plane shown in figure 3), and i is the row index of the displacement vector $\boldsymbol{u}$ and column index of the shell stiffness matrix $\boldsymbol{K}_{\text{plate}}$. The simulation process is repeated in all six deformation modes to evaluate the full stiffness matrix. Each simulation is carried out as a linear perturbation analysis; hence, a value of 1 is used for each non-zero deformation mode for simplicity. These deformation modes are shown in figure 4.

Note that additional constraints can also be used to apply pure transverse shear deformation to the unit cell to evaluate the transverse shear stiffness matrix [22]. The transverse shear stiffness matrix should ideally be evaluated for cases with low panel length-to-thickness ratios. However, as the panel length-to-thickness ratio is sufficiently high for the default configuration, and evaluating the transverse shear stiffness matrix is significantly expensive due to additional constraints required on all RVE nodes [22], this study does not explicitly evaluate the transverse shear stiffness matrix.

The geometric variables of the panel are highlighted in figure 3, and their default values and bounds for the parametric study are shown in table 3. The unit cell is generated and meshed in GMSH [33], an open-source meshing software.

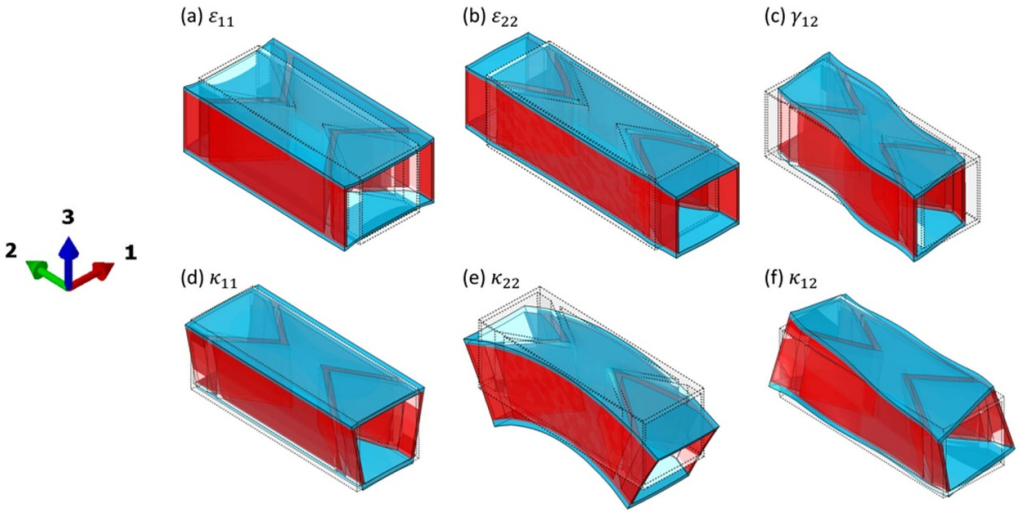

Figure 4. Deformation modes of the RVE used in the homogenisation process.

The unit cell is modelled using first-order brick elements with reduced integration (i.e. 'C3D8R' elements) as they provide converged results with a coarser mesh. An average mesh size of 1 mm is used to mesh all the unit cells. The material properties and the constraints equations are added to the input file for the Abaqus [27] FE solver, followed by the boundary conditions and the loading steps. The solid elements have 3 degrees of freedom on each node. Hence, the only boundary condition used in this case is a pin constraint on an arbitrary node without any other constraint to avoid rigid body motion. The loading steps were added as 6 different load cases, each deforming the RVE in one of the shell deformation modes (i.e. ε_{11}, ε_{22}, γ_{12}, κ_{11}, κ_{22}, κ_{12}) while the other values are zero. For each deformation mode a unit displacement is applied to the corresponding reference nodes (i.e., $u_1^{\varepsilon}, u_2^{\varepsilon}, u_3^{\varepsilon}, u_1^{\kappa}, u_2^{\kappa}, u_3^{\kappa}$) while the other reference nodes' displacements remain zero.

GMSH and Abaqus are run automatically through an application programming interface, which is compatible with Python programming language. Following the homogenisation simulation, the results are automatically extracted from the output file using a Python script and saved as a shell stiffness matrix. Hence, the full homogenisation process is automated using a bespoke Python script, enabling large batch runs and parallel processing.

2.2. *Fairing model as a shell surface*

Like the homogenisation process, the analysis of the shell fairing is repeated for various geometries of wing sections and equivalent shell properties. The process of mesh generation, FE analysis, and results extraction are therefore automated using a Python script, enabling simultaneous analysis of multiple cases. This section describes the process of generating the fairing model for FE analysis and extracting the simulation results for the parametric study.

The geometry of the wing section is defined in three steps. First, the nodes of the flared ribs are defined using analytical expressions that account for the wing's sweep angle and taper ratio. Next, the surface nodes of the ribs are offset inward in the direction normal to the surface by half the thickness of the panel. The offset nodes represent the midplane of the GATOR panel fairing, where the homogenised equivalent stiffness properties are defined. Finally, the surface geometry of the wing section is defined in GMSH using the offset nodes of the flared ribs.

Initially, a grid of normalised chord locations $\boldsymbol{x} \in [0,1]$ and spanwise rib locations $\boldsymbol{Y} \in [0,L]$ is defined at the midplane (i.e. $Z=0$) for a wing section of a given span (L). A pivot point is defined for each rib using a uniform normalised chordwise location (x_Λ) but a different spanwise location (Y_Λ). The grid points representing each rib are scaled, translated and rotated around their pivot point to account for their local chord, sweep angle, and flare angle. This transformation is carried out using the expressions in equations (3)–(5)

$$X = Y\sin\phi + xc\left(1 - \frac{Y}{L}(1-T)\right) \tag{3}$$

$$X = X_\Lambda - (Y - Y_\Lambda)\cot\Lambda \tag{4}$$

$$Y = \frac{c\left(x_\Lambda\left(1-\frac{Y_\Lambda}{L}(1-T)\right)-x\right) + Y_\Lambda(\cot\Lambda + \sin\Lambda)}{\cot\Lambda + \sin\Lambda - xc\frac{1}{L}(1-T)}. \tag{5}$$

The parameters c, ϕ and T represent the wing section's root chord, sweep angle and taper ratio, respectively. Equation (3) represents a line along the span at a given normalised chord location (x) and is used to evaluate the X coordinates of the scaled grid points. Equation (4) represents a line along the rib rotated by flare angle (Λ) about the pivot point of the rib. Combining equations (3) and (4) gives equation (5), which evaluates the Y coordinates of the transformed grid. This transformed grid is shown in figure 5(a) along with the pivot point of each rib.

The transformed grid is used with the NACA 4-digit series [33] aerofoil equations to define the nodes representing the outer surface of the ribs. These nodes of the ribs are shown

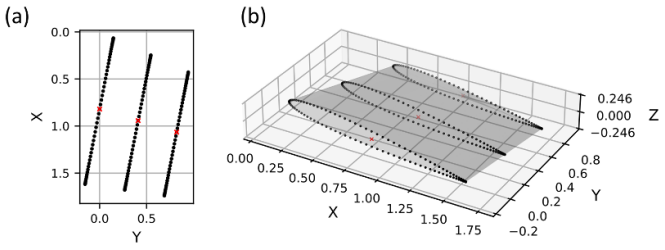

Figure 5. Fairing geometry. (a) Shows the X and Y coordinates of the scaled grid and rotated grid. (b) Shows the aerofoil nodes (i.e. Z coordinates) generated using the grid. In both figures, the red crosses represent the pivot point of the ribs.

in figure 5(b), along with the pivot points, which will be used to define the constraints for the FE simulation.

The rib nodes defined above are at the outer surface of the wing section. However, the homogenised shell stiffness is defined at the midplane of the GATOR panel. Hence, the rib nodes are offset by half the panel thickness in the direction of the inward pointing unit normal vector, as shown in equation (6),

$$P_{ij}^{\text{midplane}} = P_{ij}^{\text{surface}} + \frac{t_\text{p}}{2}\hat{n}_{ij} \quad \text{where} \quad P_{ij} = \begin{bmatrix} X & Y & Z \end{bmatrix}^\text{T}. \tag{6}$$

The variable t_p represents the thickness of the panel, $\hat{n}_{ij}$ represents the unit normal vector, and the indices i and j refer to the grid location of the node in spanwise and chordwise directions. The normal direction is derived by rotating the tangential direction of the aerofoil equation by 90 degrees, while the derivative of the aerofoil equation gives the tangential direction. The offset nodes are used to create the surface representing the midplane of the fairing panel in GMSH. The fairing surface is discretised using a structured mesh with first-order quadrilateral elements (i.e. 'S4R' elements) with an average mesh size of 20 mm.

The linear elastic constitutive properties of the shell surface are defined using the equivalent shell stiffness matrix from the homogenisation process. Abaqus further estimates a transverse shear stiffness matrix if it is not explicitly defined, as the shell element used (i.e., 'S4R') is formulated based on the Reissner–Mindlin plate. This formulation approaches the Kirchoff–Love plate formulation as transverse shear stiffness increases. The transverse shear stiffness matrix is estimated using the in-plane stiffness matrix [34], as shown in equation (7),

$$K_{11} = K_{22} = \frac{1}{6}(A_{11} + A_{22}) + \frac{1}{3}A_{66} \text{ and } K_{12} = 0 \tag{7}$$

$$\text{where} \begin{bmatrix} V_{13} \\ V_{23} \end{bmatrix} = \begin{bmatrix} K_{11} & K_{12} \\ K_{22} & K_{22} \end{bmatrix} \begin{bmatrix} \gamma_{13} \\ \gamma_{23} \end{bmatrix}.$$

The variables V_{i3} and γ_{i3} where $i \in [1, 2]$ represent distributed transverse shear force and transverse shear strain, where i is the normal direction of the RVE face. As the panel is stiff in the 2-axis, the estimated transverse stiffness is also high,

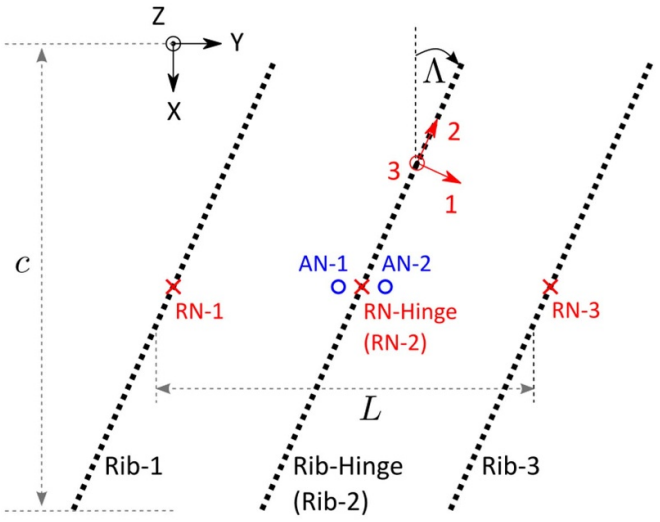

Figure 6. Schematic of the fairing variables, coordinate systems and additional nodes for constraints and loading. Nodes 'AN-1' and 'AN-2' are co-located with the point 'RN-2' (shown slightly separated for clarity). *XYZ*-axes is the global coordinate system, and 123-axes is the hinge and the material coordinate system.

thereby reducing the transverse shear deformation and making the shell deformation closer to that of the Kirchoff–Love plate formulation.

The fairing variables, coordinate systems and the additional nodes used to define the constraints are shown in figure 6.

It shows the 123-axes, which define both the hinge orientation and the orientation of the shell stiffness properties. A cylindrical coordinate system with the same directions shown in 123-axes (i.e. 1-axis being longitudinal and 2-axis being circumferential direction) is projected to the fairing surface to define material orientation on each element. The panel's stiff axis is aligned with the hinge axis, enabling the panel's flexible direction to undertake the greatest proportion of deformation due to folding. Hence, the projected 1-axis represents the morphing direction of the panel, and the 2-axis represents the stiff direction.

Additional nodes 'AN-1' and 'AN-2', shown in figure 6, are introduced to define the constraints required to model the folding wingtip. These nodes are co-located with the hinge, which is represented by the pivot point of the central rib. This pivot point of the central rib is shown as 'RN-Hinge' in figure 6. The fairing model can be reduced to a half model for wing sections symmetric across the central rib. The wing section is symmetric across the central rib for untapered and unswept wings with zero flare angle. The constraints applied to the ribs differ based on whether the model is a full model or a half model. Hence, these constraints are listed in table 5.

The rest of the constraints are applied to pivot points and the additional nodes to restrict the motion of the ribs. Firstly, the fixture of the inboard rib is enforced by fixing the node 'AN1'. Next, the co-location of 'AN-2' and 'RN-Hinge' with 'AN-1' is enforced by constraining the translation of 'AN-2' and 'RN-Hinge' to that of 'AN-1'. Similarly, the hinge connection of the wingtip and the central rib is enforced by constraining the

Table 5. Constraints applied to fairing ribs.

Full model
• The nodes of the inboard and outboard ribs are rigidly connected to 'AN-1' and 'AN-2', respectively. • The nodes of the central rib are rigidly connected to 'RN-Hinge'. • The nodes of the floating ribs are rigidly connected to their respective pivot point.
Half model
• The nodes of the inboard rib are rigidly connected to 'AN-1'. • The nodes of the central rib are rigidly connected to 'AN-2'. • The nodes of the floating ribs are rigidly connected to their respective pivot point.

rotation of 'AN-2' and 'RN-Hinge' to the hinge axis, shown as the 2-axis in figure 6. These two constraints are applied in Abaqus using the 'Join, Revolute' connector sections.

The fairing is loaded with an initial pre-tension step followed by a folding step. Pre-tension is applied to the fairing in the direction perpendicular to the hinge using artificial thermal loads. A pre-strain load vector $\boldsymbol{F}$, representing the distributed load generated on a constrained plate due to unit temperature change (ΔT), is defined with the constitutive properties of the shell section. The applied temperature change in this case is -1, and the resulting thermal load ($\boldsymbol{N}_{\text{thermal}}$) is applied to the shell elements, as shown in equation (8),

$$\boldsymbol{N} = \boldsymbol{K}_{\text{plate}}\boldsymbol{\varepsilon} - \boldsymbol{N}_{\text{thermal}} \tag{8}$$

where

$$\boldsymbol{N}_{thermal} = \Delta T\boldsymbol{F},$$
$$\boldsymbol{F} = \boldsymbol{K}_{\text{plate}} \begin{bmatrix} \varepsilon_{\text{p}} & 0 & 0 & 0 & 0 & 0 \end{bmatrix}^{\text{T}}.$$

The wingtip folding deformation is applied as rotation to the node 'AN-2'. Note that the nodes 'RN-Hinge' and 'AN-2' are constrained to rotate only about the hinge axis. As a result of this constraint, a rotation of the node 'AN-2' defined around the global X-axis will also result in a rotation around the global Y-axis to ensure the overall rotation of the node is always around the hinge axis. Hence, for simplicity, rotation is applied to the FE model as an X-axis rotation on 'AN-2', and the resulting reaction moment is also measured around the X-axis. This rotation and moment around the global X-axis are resolved to rotation and moment around the hinge axis using equations (9) and (10).

$$\theta = \frac{\theta_X}{\cos\Lambda} \tag{9}$$

$$M = \frac{M_X}{\cos\Lambda}. \tag{10}$$

Note that the applied rotation angle is different for the full and half model of the fairing. In the full model, folding rotation (θ) is applied to the outboard rib through the node 'AN-2', effectively rotating the entire section outboard of the hinge (i.e. the wingtip). In a symmetric wing section, the consequent rotation of the central rib is always half of the folding angle of the wingtip. Hence, in a half model, half the folding angle of the wingtip is applied to the central pivoting rib, again through the node 'AN2', to achieve equivalent fairing deformation. This rotation applied to the central rib of the half model is hereafter referred to as the rotation angle $\left(\frac{\theta}{2}\right)$.

For instance, consider a full model simulation of the baseline fairing at an 80-degree folding angle of the wingtip, shown in figure 7.

The deformation at the inboard region up to the central rib is identical to that of a half model with a 40-degree rotation angle applied to the central pivoting rib. However, the half model would produce half the reaction moment compared to the full model. Hence, the reaction moment from the half model should be doubled before comparing it to that of the full model. All the fairing configurations analysed in this study are symmetric about the central pivoting rib. Hence, they are analysed using the half model, thereby significantly reducing the FE simulation time.

2.3. Method validation with a simplified geometry

The two-scale modelling approach is validated by comparing its results with a full-scale model for a simplified geometry. A fairing slice along the span is modelled at the thickest chordwise location of the aerofoil (i.e. at 30% chord for NACA 0015 aerofoil), where the deformation is greatest. This slice has a width of 1 cell (i.e. 35.9 mm) in the chordwise direction and a span of half model of the fairing (i.e. 400 mm). The chordwise ends of the slice are free, while the boundary conditions at the spanwise ends are the same as the fairing half model described in table 5. The results presented show the disparity between the two-scale and full-scale models due to the assumption of linear elastic stiffness properties for the shell elements.

Two cases were used in this study, one without pre-strain and the other with 10.3% pre-strain. For the shell model, pre-strain was applied using a thermal load, as described for the wing model in section 2.2. The full-scale model without pre-tension has 32 cells along the span. For the full-scale model with 10.3% pre-strain, the pre-strain was applied by defining 29 cells (i.e. 362.5 mm) along the span and stretching it to the span of the half model (i.e. 400 mm). A rotation was applied to both models, and their reaction torques were measured as described in section 2.2. The deformed shape of the full-scale model with 10.3% pre-strain and the torque response of all two-scale and full-scale models are shown in figure 8.

Figure 8(b) shows close agreement between the two-scale and the full-scale models where the strains are relatively low. For the model without pre-strain, the error in the shell model relative to the full-scale model at 20-degree rotation is 3.2%. The error is slightly higher, at -9.4% for the case with 10.3% pre-strain at 20-degree rotation. This increase in error is due to the changes in the stiffness properties of the sandwich panel at high strain states. As the shell model assumes linear elastic stiffness properties, it does not capture the effects of stiffness changes in the sandwich panel due to geometric nonlinearity in the deformation.

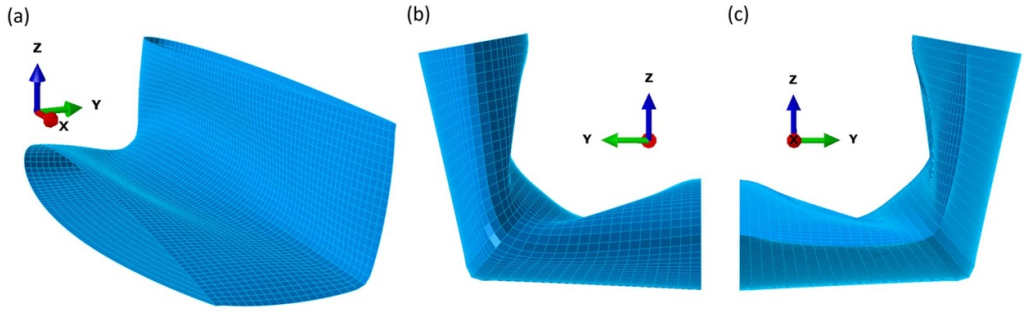

Figure 7. Deformed shape of the fairing full model at 80-degree rotation of the wingtip. (a) Shows the 3-dimensional view, (b) the leading-edge view, and (c) the trailing-edge view of the fairing.

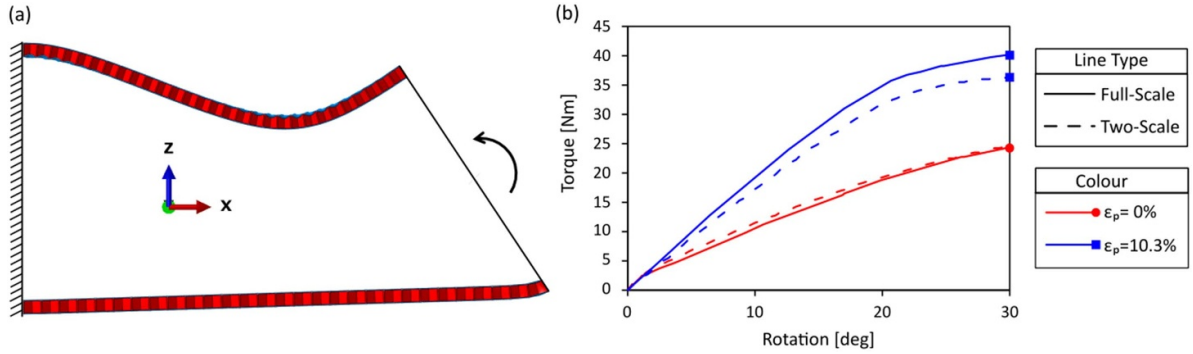

Figure 8. Comparison of full-scale and two-scale models for a simple geometry. (a) Shows the deformed shape of the full-scale mode with 10% pre-strain, and (b) shows the torque response for the applied rotation.

Despite the small error introduced by the shell model due to assumed linear elastic stiffness properties, it captures the effect of pre-strain comparable to the trends shown by the full-scale model. In both models, torque increases due to the applied pre-strain relative to the case without pre-strain, indicating the effect of the design variable on the performance objective. Hence, the two-scale model offers a practical analysis approach for a parametric design study at a fraction of the computational cost relative to the full-scale model.

2.4. Metrics for fairing objectives

The study aims to identify the geometric features which improve the objectives of reducing the torsional stiffness of the joint and cross-section distortion of the fairing. Hence, these objectives must be quantified to compare the effect of various design variables on them. The reaction torque on the joint at a prescribed rotation angle is used to represent torsional stiffness, and it is evaluated from the FE results using the expression in equation (10). In contrast, the distortion of the fairing is visually noticeable, as shown by the deformed baseline fairing in figure 6. However, they are difficult to quantify as there is no *a priori* known desired shape to calculate the difference between a deformed shape and a desired shape in the simulation. Instead, three different metrics are studied to quantify the cross-section distortion. These metrics are based on three physically meaningful quantities integrated over the fairing surface, namely energy, curvature, and displacement, as defined in equations (11)–(13),

$$\text{Energy metric} = \frac{\Delta J_{\text{in-plane}}}{\Delta J_{\text{out-of-plane}}} = \frac{\Delta\left(\frac{1}{2}\sum_{\text{e}} A\left(\boldsymbol{N}\cdot\boldsymbol{\varepsilon}\right)\right)}{\Delta\left(\frac{1}{2}\sum_{\text{e}} A\left(\boldsymbol{M}\cdot\boldsymbol{\kappa}+\boldsymbol{V}\cdot\boldsymbol{\gamma}\right)\right)} \tag{11}$$

$$\text{Curvature metric} = \sqrt[2]{\frac{\sum_{\text{e}} A\left(\kappa_1^2+\kappa_2^2\right)}{\sum_{\text{e}} A}} = \sqrt[2]{\frac{\sum_{\text{e}} A\left(\kappa_{11}^2+\kappa_{22}^2+\frac{1}{2}\kappa_{12}^2\right)}{\sum_{\text{e}} A}} \tag{12}$$

$$\text{Displacement metric} = \frac{1}{n_{\text{b}}}\sum_{i}^{n_{\text{b}}} u_{3i} - \frac{1}{n_{\text{t}}}\sum_{j}^{n_{\text{t}}} u_{3j}. \tag{13}$$

Equation (11) shows the energy metric, representing the ratio of incremental change in the strain energy due to in-plane and out-of-plane deformations. The summation is over all shell elements, and the variable A represent element area. The variables $\boldsymbol{N}$, $\boldsymbol{M}$ and $\boldsymbol{V}$ are the vectors of distributed in-plane forces, out-of-plane moments and transverse shear forces of shell elements, respectively. The variables $\boldsymbol{\varepsilon}$, $\boldsymbol{\kappa}$ and $\boldsymbol{\gamma}$ are the vectors of in-plane strains, out-of-plane curvatures and transverse shear strains of shell elements, respectively. The equation shows that the out-of-plane deformation energy includes bending and transverse shear deformation energies. However, the transverse shear deformation energy contributes less than 5% of

the total out-of-plane deformation energy in all the cases considered in this section. Hence, the transverse shear deformation has a negligibly small effect on the energy metric.

Equation (12) shows the curvature metric, representing an area-weighted root mean square (RMS) of principal curvatures of the shell surface. The principle curvatures are annotated as κ_1 and κ_2. However, for simplicity, the equivalent expression of engineering curvatures κ_{11}, κ_{22} and κ_{12} of the shell element are used to evaluate the metric.

Equation (13) shows the displacement metric, representing the difference in the average vertical displacement of the nodes on the bottom and top surfaces of the fairing. For the half model used in the analysis, this metric represents the average reduction in the thickness of the wing section. In this case, the summations are over the vertical displacement of the nodes in the bottom and top surface. The variable n_b and n_t represent the number of nodes in the bottom and top surface, respectively.

In order to have an initial understanding of the response of the fairing and the usefulness of the performance metrics, the effects of increasing the number of floating ribs on three different magnitudes of fairing rotation are studied, as shown in figure 9.

It shows the folding response of the fairing for different metrics alongside snapshots of the deformed shape at various rotation angles. Note that the results presented are for a half model; hence, the 40-degree rotation angle of the pivoted rib is equivalent to an 80-degree folding angle of the wingtip. The number of floating ribs (n_{fr}) is changed between the cases, leading to a different unsupported panel length between the ribs. Adding floating ribs (n_{fr}) reduces the cross-section distortion of the fairing but at the cost of increased torsional stiffness of the joint. The top graph in figure 9(a) shows the increase in torque with the number of floating ribs (n_{fr}). The middle and bottom graphs show the effect of the number of floating ribs (n_{fr}) on the metrics considered to quantify the cross-section distortion of the fairing.

The middle graph in figure 9(a) shows the energy metric normalised by its initial value for each case. It shows a steep drop in the metric as the fairing undergoes large out-of-plane deformation due to buckling of the top skin between 20 to 30 degrees of rotation. This sharp drop in the metric aligns with the softening of the torque gradient in the top graph of figure 9(a), indicating a drop in stiffness. It further aligns with the significant increase in cross-section distortion shown between the same rotation angles in figure 9(b). Hence, the normalised energy metric is useful in indicating the rotation angle beyond which the cross-section gets distorted significantly due to the buckling of the top skin.

The in-plane and out-of-plane components of strain energy increase with the number of floating ribs, as shown in the middle graph of figure 9(a). In contrast, figure 9(b) shows reduced cross-section distortion with more floating ribs (n_{fr}). The increase in out-of-plane strain energy is due to the increase in the number of rib bays, each with a similar deformation mode shape to that of the fairing with no floating ribs (n_{fr}). Hence, the 'wavelength' of the out-of-plane deformation decreases with the floating ribs (n_{fr}), leading to increased curvature, as shown by the curvature metric in the bottom graph in figure 9(a). The curvature increase on the fairing increases the out-of-plane strain energy for the fairing with more floating ribs (n_{fr}), despite it reducing the distortion of the fairing. The reduced out-of-plane displacement with more floating ribs (n_{fr}), as shown in figure 9(b), further results in greater in-plane displacement (e.g. more compression on top surface), thereby increasing the in-plane strain energy.

The curvature metric is useful for comparing the effects of design variables on the fairing objectives for cases with a constant number of floating ribs. Authors previously used a curvature-based metric to compare the effects of sandwich panels with positive, negative and zero Poisson's ratio core on the fairing objectives [20]. The displacement metric shown in the bottom graph of figure 9(a) further compares the effects of floating ribs on the fairing distortion. The figure shows that the displacement metric decreases with more floating ribs (n_{fr}), which is consistent with the deformed shapes shown in figure 9(b). Moreover, similar to the normalised energy metric, the displacement metric shows a change in the gradient where the out-of-plane displacement of the fairing rapidly increases due to the buckling of the top skin. This change gradient in the displacement metric aligns with the softening of the torque gradient, indicating a drop in stiffness.

Each metric provides some insights into the effects of the design variable on the fairing objectives. The normalised energy metric indicates the rotation angle at which the top skin buckles and the curvature metric indicates the out-of-plane deformation as the wingtip folds. However, in the case of varying numbers of floating ribs, their trends are inconsistent with the visually observed distortion of the fairing shape. In contrast, the displacement metric indicates out-of-plane deformation as the wingtip folds and the rotation angle at which the top skin buckles. Its trends are consistent with the visually observed distortion of the deformed fairing shape. Hence, the displacement metric offers a robust measure that better represents the distortion of the cross-section shape for this parametric study.

In the rest of the study, the reaction torque is used to measure torsional stiffness and the displacement metric is used to measure fairing distortion as the wingtip folds. These metrics are used in the following section to study the sensitivity of the objectives to each design variable and the trends of the objectives with the design variables that strongly affect them.

3. Results and discussion

Two types of analyses are carried out using the models presented above. First, a sensitivity study of the fairing objectives is presented for each design variable. This study enables the variables that strongly affect the objectives to be selected for more detailed parametric studies, thereby reducing the design space. In the parametric study, a pair of variables strongly affecting at least one of the objectives are studied to identify the trends and the ranges of design variable values that reduce trade-offs between the objectives. The parametric study focuses on

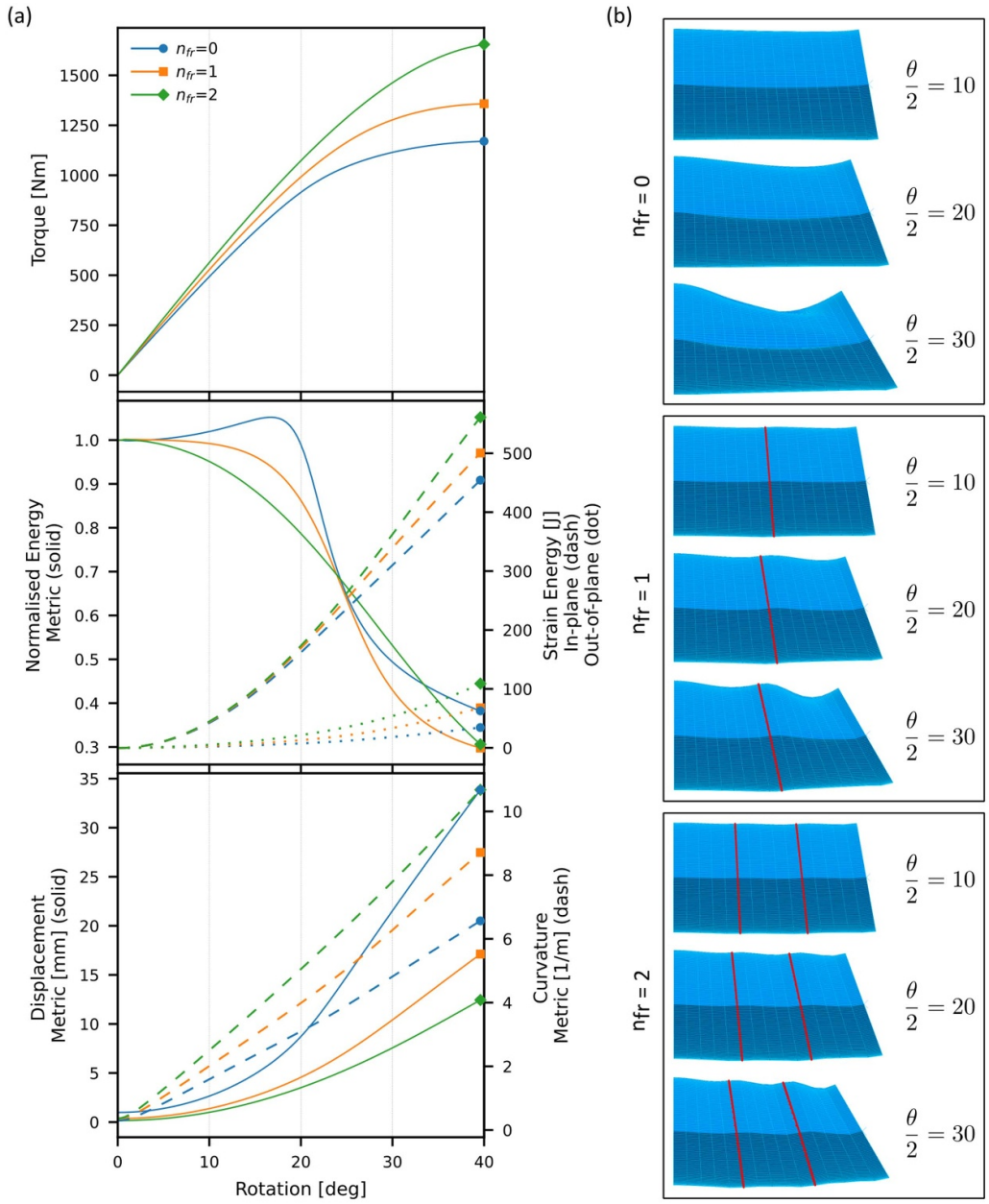

Figure 9. Various metrics used to quantify the objectives for cases with varying numbers of floating ribs (n_{fr}). (a) Shows the response of the metric for a half model. (b) Shows snapshots of deformed shapes from the rear of the wing at various rotation angles.

the panel layer thicknesses, chevron geometry and the fairing variables. Moreover, considering the buckling of the top skin between 20–30 degrees of rotation, as shown in figure 9, the results presented for the parametric study use the torque and distortion metric values from 20-degree rotation.

3.1. Sensitivity study

In the parametric study, each design variable is swept through a set of values uniformly distributed between the limits shown in tables 3 and 4 for panel and fairing variables. Ten sample points are used for each panel variable, while five are used for each fairing variable (except for the number of floating ribs, which has 3 discrete values). The sensitivity of each objective to the variation in each design variable is evaluated by calculating the range of variation in the objective value as a percentage of its value in the baseline configuration. The expression for sensitivity value is shown in equation (14), where the objective value is shown as O_i with i referring to minimum, maximum or default value,

$$\text{Sensitivity} = \frac{O_{\max} - O_{\min}}{O_{\text{default}}}. \tag{14}$$

The evaluated sensitivity of the metrics to changes in each design variable is shown in figure 10.

Figure 10 shows that all the panel variables significantly influence torque (>5%), with facesheet thickness (t_{f}) having the predominant effect, followed by the chevron dimensions.

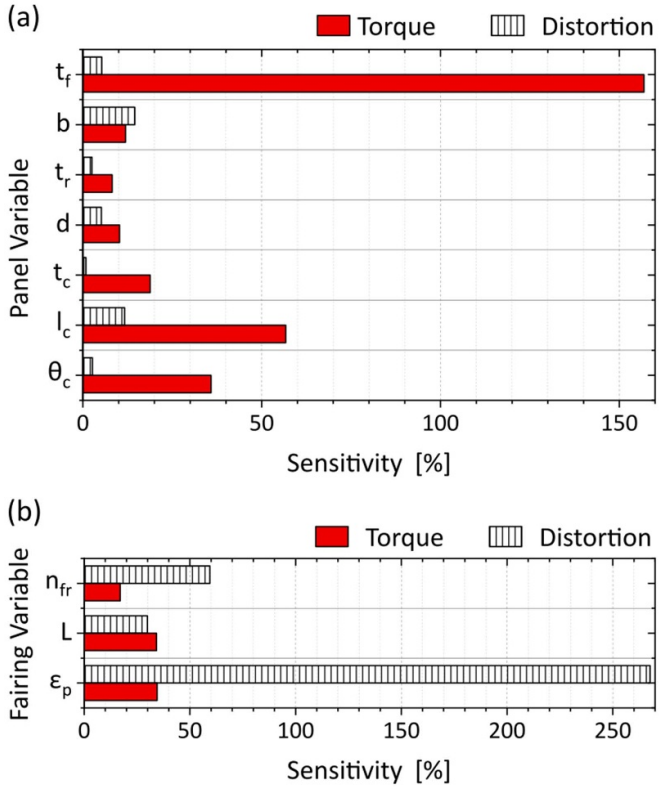

Figure 10. Sensitivity of the objectives to changes in each variable. Torque and distortion are for the 20-degree rotation of the half model.

Chevron length (l_c) has the dominant influence from the chevron dimensions, followed by the chevron angle (θ_c) and thickness (t_c). For all the panel variables except the core thickness (b), their effect on the distortion metric is much smaller than their effect on torque. The core thickness (b) and the chevron length (l_c) significantly influences the distortion metric, with the influence of the other variables being relatively small ($\leqslant$ 5%). In contrast, all the fairing variables show a strong influence on both objectives, with the number of floating ribs (n_{fr}) and the pre-strain across the hinge (ε_p) having the dominant effect on the distortion metric, followed by the fairing span (L). The observations from the sensitivity study enable the reduction of the design space by eliminating the variables that do not significantly influence the objectives. The following parametric study of the influential variables shows the trends of the objectives and useful ranges of the variable values that improve the objectives.

3.2. Panel layer thicknesses

In the parametric study, a variable that strongly influences an objective is paired with another variable that strongly influences the other objectives to explore the feasibility of decoupling the objectives and reducing their trade-off. The core thickness (b) strongly influences the distortion metric, with a smaller effect on the torque. In contrast, the facesheet thickness (t_f) strongly influences torque with negligible effect on distortion. Hence, the core thickness (b) paired with the facesheet thickness (t_f) offers a relatively decoupled design space to improve both objectives.

The torque and distortion responses for various core thickness (b) and facesheet thickness (t_f) values are shown in figure 11(a).

For comparisons between the cases, the torque and distortion values are shown for a rotation angle of 20 degrees before the onset of top skin buckling. The blue lines show steep reductions in distortion with relatively modest increases in torque for increasing core thickness (b). The red lines show large increases in torque with relatively small increases in distortion for increasing facesheet thickness (t_f). These effects on the fairing objectives are related to the changes in the panel's axial stiffness and bending rigidity in the morphing direction (i.e. 1-axis). The panel's axial stiffness and bending rigidity for a nominal 1 $\times$ 1 m flat panel are shown in equations (17) and (18), respectively,

$$\text{Axial Stiffness} = t_p E_1 \tag{15}$$

$$\text{Bending Rigidity} = \frac{t_p^3 E_1^D}{12}. \tag{16}$$

The variable t_p is the panel thickness, E_1 is the equivalent modulus from the in-plane stiffness matrix (i.e. **A**-matrix), and E_1^D is the equivalent modulus from the out-of-plane stiffness matrix (i.e. **D**-matrix).

Figure 11(b) shows the axial stiffness and bending rigidity in the morphing direction for various core (b) and facesheet thicknesses (t_f). The blue lines show large increases in bending rigidity with increasing core thickness (b), which consequently reduces the fairing distortion. The red lines show large increases in the axial stiffness with increasing facesheet thickness (t_f), which increases torque. The red lines further indicate that increasing facesheet thickness (t_f) only increases in-plane stiffness for panels with thin cores, while it increases both in-plane stiffness and bending rigidity for panels with thick cores. In panels with thick cores, the facesheets are further away from the midplane; hence, any increase in facesheet thickness (t_f) significantly increases bending rigidity. However, increasing facesheet thickness in panels with thick cores does not reduce distortion, as shown in figure 11(a), despite increasing bending rigidity. Instead, increasing facesheet thickness (t_f) shows a slight increase in distortion for all core thicknesses (b) due to the simultaneous increase in the axial stiffness. Increasing axial stiffness favours bending deformation of the top skin over large compressive deformations, thereby increasing the distortion. Hence, the best solution for the fairing objectives is a GATOR panel with a thick core and thin facesheets, which improves bending rigidity and axial flexibility, respectively. In contrast, the worst combination is having a thin core and thick facesheets. Figure 11(c) shows the 13-plane view of these panel geometries.

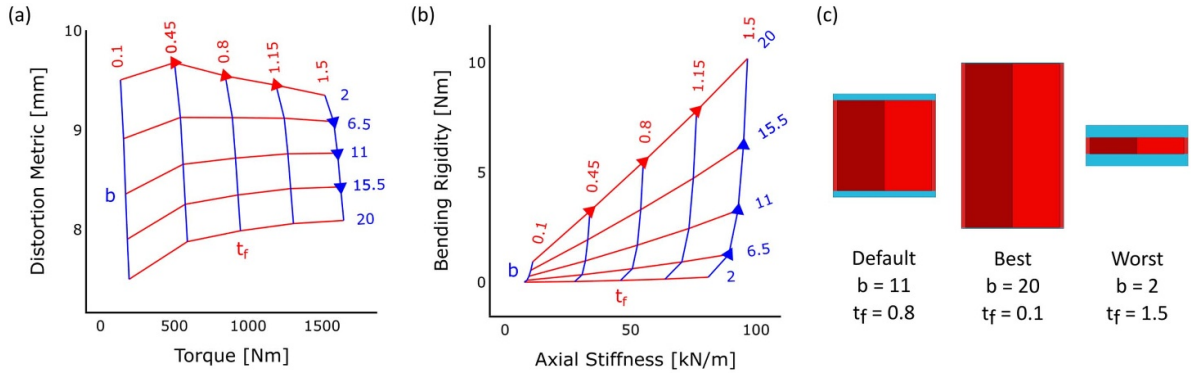

Figure 11. Parametric study of core thickness (b) and facesheet thickness (t_f). (a) Shows the torque and distortion response for a 20-degree rotation of the pivoted rib. (b) Shows the equivalent axial stiffness and bending rigidity in the morphing direction. (c) Shows the geometry of the notable cases (13-plane view).

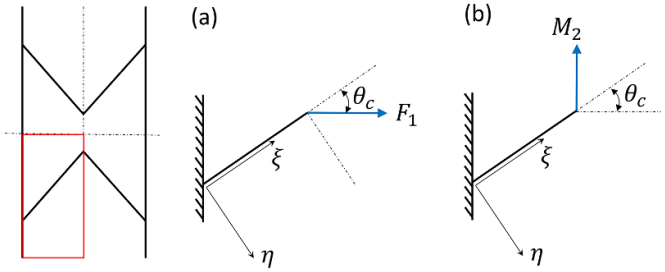

Figure 12. Loading diagram for analytical expressions.

3.3. Chevron geometry

The deformation of the sandwich panel is complex due to the interaction of the facesheets and the chevrons. However, the trends in the stiffness properties due to the changes in the chevron geometry can be explained using the mechanics of the chevron deformation. Consider the axial and bending deformation of the core in the 1-axis shown in figure 12.

The corresponding analytical expressions for axial [29] and bending [35] displacements of the chevron walls are shown in equations (17) and (18), where k and q are shear (typically $k = 2.4 + 1.5\nu$) [36] and torsional [34] coefficients respectively, and K and I are polar and area moments of inertia,

$$\delta_1 = \frac{F_1 l_c}{Ebt_c}\left[\left(\frac{l_c}{t_c}\right)^2 \sin^2\theta_c + k\sin^2\theta_c + \cos^2\theta_c\right] \tag{17}$$

$$\theta_2 = M_2 l_c\left[\frac{q}{KG}\sin^2\theta_c + \frac{1}{EI}\cos^2\theta_c\right]. \tag{18}$$

The terms in the square bracket in equation (17) correspond to the chevron's bending, transverse shear and axial deformation, respectively. The $\sin^2\theta_c$ values increase with increasing chevron angle (θ_c) while the $\cos^2\theta_c$ values decrease. Hence, the chevron's bending and transverse shear displacements increase while its axial displacement decreases with larger chevron angles (θ_c). The expression further indicates that the bending displacement increases significantly with the slenderness (length-to-thickness ratio) of the chevrons. The increasing bending displacement reduces the relative contribution of the chevron's transverse shear deformation to panel displacement, hence reducing the chevron's transverse shear stiffness contribution to the equivalent axial stiffness of the panel. Furthermore, the terms in the square bracket in equation (18) correspond to the chevron's torsional and transverse bending deformation, respectively. The expression indicates that the chevron's rotation due to torsion increases while its rotation due to transverse bending decreases with larger chevron angles (θ_c). The torsional coefficient (q) decreases from unity with the increasing height-to-length ratio of the wall [35, 37, 38], thereby reducing the torsional stiffness for longer chevrons. These analytical trends are used in the following discussion to contextualise the effects of the chevron geometry on the FE-generated stiffness properties shown in figures 13 and 14.

The red lines in figure 13(a) show a large decrease in torque for the initial increase in the chevron length (l_c), followed by smaller reductions for subsequent increases. The large initial decrease in torque is attributed to the large initial drop in the panel's axial stiffness, as shown in figure 13(b), due to the reduced stiffness contribution from the chevron's transverse shear stiffness. Once the chevron's transverse shear stiffness contribution is negligible, typically for a slenderness ratio greater than 15, the incremental reductions in the panel's axial stiffness with increasing chevron length (l_c) becomes very small. Consequently, a further increase in chevron length (l_c) provides only a smaller reduction in torque for panels with long chevrons. Moreover, the red lines in figure 13(a) indicate that distortion of the fairing increases with longer chevrons (l_c). This increase in distortion is due decreasing bending rigidity of the panel, as shown by the red lines in figure 13(b), particularly for thicker cores. This trend is attributed to the reduction in the chevron's torsional stiffness due to the decreasing height-to-length ratio of the chevron wall.

The blue lines in figure 13(a) further show that while the effect of increasing core thickness (b) is predominantly on distortion, for short chevrons, it also increases torque. This increase in torque is due to increasing axial stiffness from thicker cores when combined with short chevrons, as shown by the rightmost blue line in figure 13(b). Short chevrons undergo a larger proportion of transverse shear deformation relative

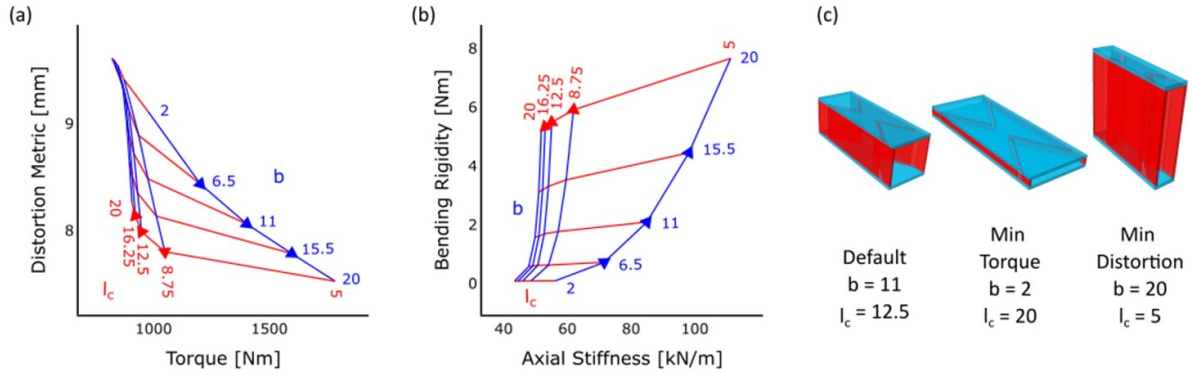

Figure 13. Parametric study of core thickness (b) and chevron length (l_c). (a) Shows the torque and distortion response for a 20-degree rotation of the pivoted rib. (b) Shows the equivalent in-plane stiffness and bending rigidity in the morphing direction. (c) Shows the geometry of the notable cases.

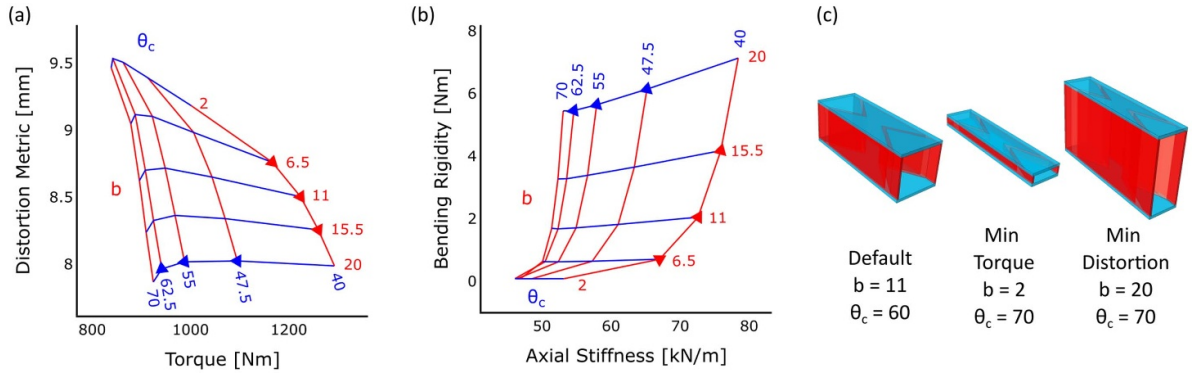

Figure 14. Parametric study of core thickness (b) and chevron angle (θ_c). (a) Shows the torque and distortion response for a 20-degree rotation of the pivoted rib. (b) Shows the equivalent in-plane stiffness and bending rigidity in the morphing direction. (c) Shows the geometry of the notable cases.

to longer chevrons when the panel is deformed axially in the morphing direction. Hence, increasing core thickness (b) amplifies the panel's high axial stiffness due to the chevron's transverse shear stiffness by increasing the cross-section area of the chevrons.

The effects of the chevron angle (θ_c) on the stiffness properties of the panel and the fairing objectives are shown in figure 14. The blue lines show a decreasing incremental reduction in torque and axial stiffness with a uniform increase in chevron angle (θ_c). This trend agrees with equation (17), which indicates that the chevron's displacement contribution of bending and transverse shear deformation increases while the contribution of the chevron's axial deformation decreases with larger chevron angles (θ_c). Moreover, in equation (17) the bending and transverse shear contribution is proportional to $\sin^2\theta_c$ whose gradient decreases from 45 to 90 degrees. This decreasing gradient results in a decreasing step change in axial stiffness with a uniform increase in chevron angle (θ_c), as shown by the blue lines in figure 14(b). The decreasing axial stiffness of the panel with larger chevron angles (θ_c) results in the decreasing torque shown in figure 14(a). Hence, both trends share the pattern of decreasing incremental reductions for uniform increases in chevron angle (θ_c).

The blue lines in figure 14(b) show decreasing bending rigidity with larger chevron angles (θ_c), particularly for thick cores. Note that the transverse bending stiffness of the chevron wall is proportional to the cube of the core thickness (b^3) due to the area moment of inertia. Hence, the chevron's transverse bending stiffness is significant for thick cores, and its contribution to the panel's bending rigidity decreases with increasing chevron angle (θ_c), as indicated by equation (18), resulting in decreasing bending rigidity. While the reducing bending rigidity does not translate to consistent trends in distortion metric in figure 14(a), it shows a consistent drop in distortion metric for high values of chevron angles (θ_c) with no corresponding increase in bending rigidity in figure 14(b). Similar to the facesheet thickness (t_f) in figure 11, this trend is attributed to the reducing axial stiffness of the panel, which enables greater in-plane compression of the top skin before increasing out-of-plane deformation, thereby resulting in a reduced distortion of the fairing. Hence, the distortion metric is affected not only by the panel's bending rigidity but also by its axial stiffness, as the skin deformation favours the lower energy deformation mode between the in-plane and out-of-plane deformation.

3.4. Fairing variables

The fairing variables strongly affect both fairing objectives, as indicated by the sensitivity in figure 10. The effects of floating ribs (n_{fr}) and the fairing span (L) are shown in figure 15.

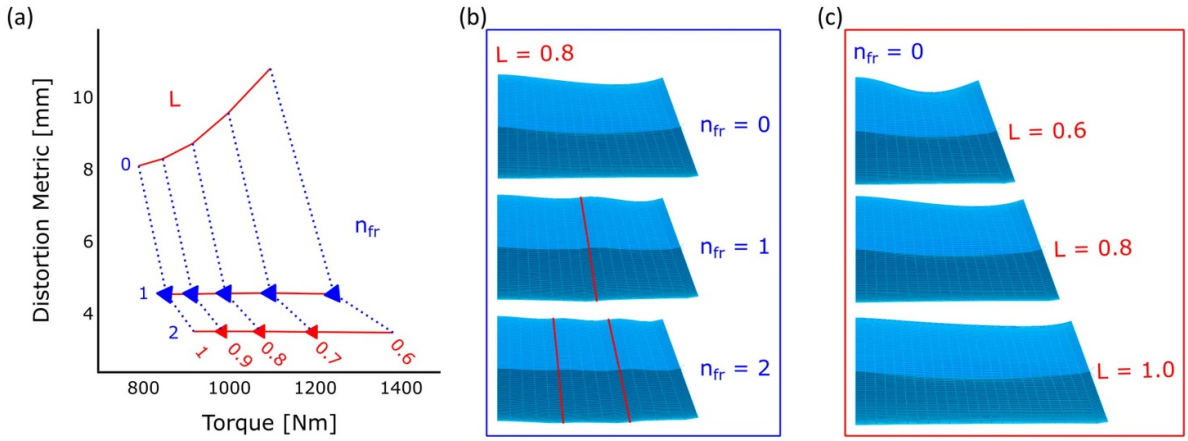

Figure 15. Parametric study of fairing span (L) and floating ribs (n_{fr}). (a) Shows the torque and distortion response for a 20-degree rotation of the pivoted rib. (b) and (c) show the corresponding deformed shape from the rear view of the fairing.

The blue dotted lines show that adding the first floating rib reduces the distortion significantly, with a smaller subsequent reduction with additional floating ribs (n_{fr}). Floating ribs (n_{fr}) reduce the unsupported length of the skin between the ribs, as shown in figure 15(b), resulting in reduced out-of-plane deformation of the panel. Floating ribs further maintain the cross-section thickness at their locations, thereby constraining the fairing deformation. This constrained fairing deformation adds stiffness to the fairing, increasing the torque with increasing floating ribs (n_{fr}). The red lines indicate that the increase in torque due to the floating ribs (n_{fr}) can be offset by increasing the span (L) of the fairing. A longer fairing section reduces the overall axial strain (i.e. 1-axis strain) by distributing the displacement over a longer length, thereby reducing the axial stiffness of the skin and, therefore, the resulting torque. This reduction in axial strain delays out-of-plane deformation of the top skin, thereby significantly reducing distortion for the fairing without a floating rib, as shown in figure 15(c). However, in the fairings with floating ribs, the out-of-plane deformation of the fairing is already reduced by the floating ribs; hence, figure 15(a) shows that further reduction in distortion due to the span (L) increase is negligibly small. Therefore, a long span (L) with few floating ribs (n_{fr}) is desired to achieve a balanced solution for both objectives.

Pre-strain (ε_p) on the fairing in the direction perpendicular to the hinge (i.e. 1-axis) delays the onset of compressive strains on the top skin as the wingtip folds. Large compressive stress on the top skin may trigger panel buckling, which distorts the cross-section shape due to large out-of-plane deformation. Figure 16 shows the effects of pre-strain (ε_p) on the torque and distortion response of the fairing.

Figure 16(a) shows that in a fairing with no pre-strain, the top skin undergoes compression from the start of folding, leading to the early buckling of the top skin, indicated by the jump in the distortion metric. Buckling of the top skin reduces the torsional stiffness but at the cost of a severely distorted cross-section, as shown in figure 16(c). The applied pre-strain (ε_p) delays the onset of buckling as a pre-tensioned top skin can withstand greater compression before encountering compressive strain. This delay in buckling extends the linearity in the fairing deformation, as shown in figure 16(a). It also shows that pre-strain (ε_p) reduces the torsional stiffness in the linear response of the fairing. This trend agrees with the 2-dimensional analytical results presented by the authors in a previous study on the effects of pre-tensioned skin over a hinged wingtip with multiple pivoted rib supports [10]. Furthermore, buckling of the top skin qualitatively changes the torque and distortion metric response, as indicated by figure 16(b). It shows that the 0% pre-strain (ε_p) case deviates from the general trend at the beginning, followed by the 5% pre-strain (ε_p) case after 10 degrees of rotation and the 10% pre-strain (ε_p) case after 20 degrees. Hence, in the following parametric studies, which include changing the pre-strain, the trends in the objectives are studied considering the region before and after buckling of the top skin.

Figure 17 shows the effects of varying the fairing span (L) and the number of floating ribs (n_{fr}) with various pre-strain (ε_p) across the hinge.

The effects of varying pre-strain (ε_p) and span (L) on torque and distortion are shown in figure 17(a). The red lines show decreasing torque and distortion for increasing pre-strain (ε_p) above 5% for the 10-degree rotation angle. In contrast, for the 20-degree rotation angle, this trend is observed for pre-strain (ε_p) above 10% due to the buckling of the top skin in the 5% pre-strain (ε_p) cases before the 20-degree rotation. In the post-buckling results shown for 20-degree rotation for pre-strains (ε_p) below 10%, increasing pre-strain (ε_p) increases the torque while reducing distortion. Moreover, the blue lines show decreasing torque with increasing span (L) for all cases. It also shows a subtle reduction in distortion with longer spans (L) for all pre-strained cases. In contrast, the distortion metric increases with the span (L) for cases without pre-strain. Hence, these results indicate the benefits of increasing pre-strain (ε_p) and span (L) to reduce both torque and distortion of the fairing.

The effects of pre-strain (ε_p) on fairings with various numbers of floating ribs (n_{fr}) are shown for a 20-degree rotation in figure 17(b). The blue dotted lines show reducing distortion and increasing torque with increasing floating ribs (n_{fr}).

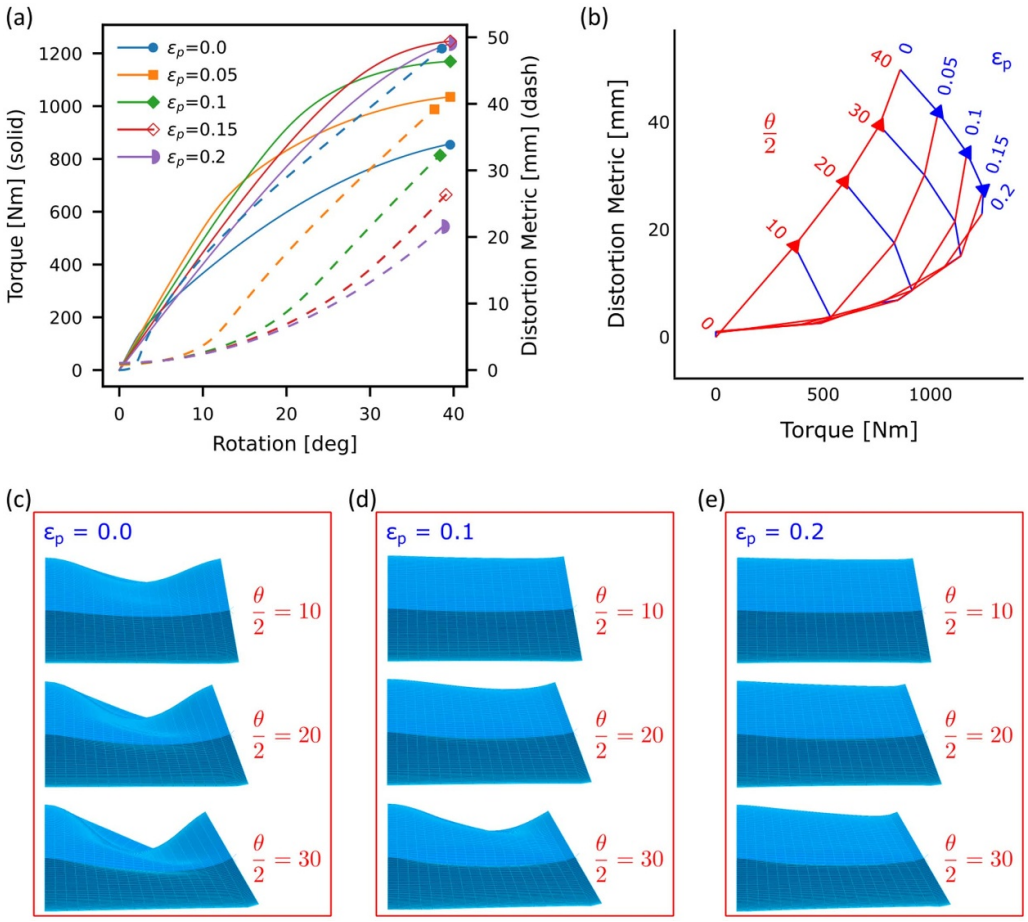

Figure 16. Parametric study of pre-strain (ε_p). (a) Shows the torque and distortion response for a 20-degree rotation of the pivoted rib. (b) Shows the deviation of the fairing response at various rotation angles for different pre-strains (c)–(e) show the deformed shapes from the rear view of the fairing.

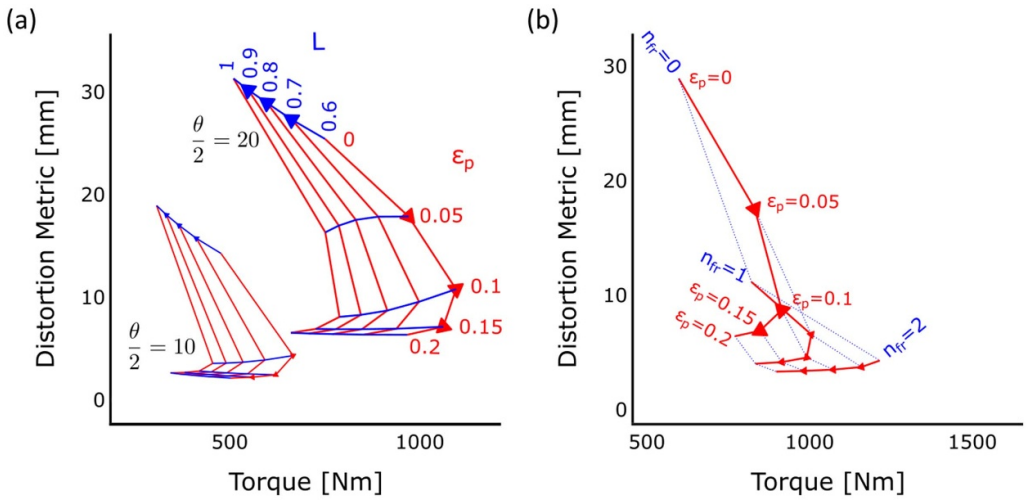

Figure 17. Parametric study of pairs of fairing variables showing the torque and distortion response. (a) Shows the effects of varying pre-strain (ε_p) and fairing span (L) for 10 and 20-degree rotation of pivoted rib. (b) Shows the effects of varying pre-strain (ε_S) and the number of floating ribs (n_{fr}) for 20-degree rotation of pivoted rib.

The red lines change direction for the cases with zero and one floating rib, indicating the onset of buckling before 20-degree rotation for cases with less than 10% and 5% pre-strain, respectively. The other red line (i.e., for two floating ribs case) shows that the buckling of the top skin can be avoided by constraining the fairing deformation with more floating ribs (n_{fr}),

thereby giving a consistently low distortion for these cases. It also shows that increasing torque due to more floating ribs (n_{fr}) can be offset using pre-strain, similar to the effects of increasing the span (L) shown in figure 15. Therefore, the combined effects of these fairing variables can improve both objectives while minimising their trade-offs.

3.5. Key insights

The sensitivity study identified the design variables that significantly influence the fairing objectives of reducing torque and cross-section distortion. Hence, the subsequent parametric study focused on these design variables, thereby significantly reducing the design space. For instance, consider pairing each panel variable with every other panel variable to produce carpet plots similar to the one presented in the parametric study. This approach would produce 21 different pairs of panel variables, each with 5 $\times$ 5 sample points (i.e. 525 simulations). In contrast, by considering the design variables that strongly affect at least one fairing objective and pairing each of these variables with variables that strongly affect the other objective, the parametric study of the panel variable was reduced to 4 different pairs (i.e. 100 simulations). Additionally, the sensitivity study used 10 sample points of each of the 7 panel variables (i.e. 70 simulations). Hence, this approach reduced the number of simulations required for the study by 68% relative to studying every possible pair.

The parametric study of the panel layer thicknesses indicated that the GATOR sandwich panels with thick cores and thin factsheets increase bending rigidity without a notable penalty to the axial flexibility in the morphing direction, agreeing with the previous analytical [19], FEM [23] and experimental [18] studies. The novelty of this study is in determining the relationship between panel design variables and the behaviour of the folding wingtip fairing through their effects on the panel's axial stiffness and bending rigidity. A systematic study of the 3-dimensional fairing in a reduced design space was presented in pairs of design variables that predominantly affect different fairing objectives. It highlighted a relatively weak coupling between the fairing objectives for changing core and facesheets thicknesses. The core thickness predominantly affects distortion, while facesheet thickness predominantly affects torque, with a relatively small influence on the other objective. This context enables the core thickness to be increased to reduce distortion with only a small penalty on torque and the facesheet thickness to be reduced to reduce torque with only a small penalty on distortion. Hence, an improved configuration relative to the baseline will have a core thickness of 11–20 mm and a facesheet thickness of 0.1–0.8 mm.

The parametric study of the chevron geometry highlighted the relationship between the analytical expressions for the core's in-plane [29] and out-of-plane [35] displacements in the morphing direction with the observed trends in the FE studies. It highlighted that for the plate's in-plane deformation in the morphing direction, a large chevron angle reduced the contribution from the chevron's in-plane (i.e. axial stretching/compression) deformation while increasing the contribution from the chevron's out-of-plane (i.e. bending and transverse shear) deformation. As the out-of-plane stiffness of the chevon is much lower than its in-plane stiffness, a high chevron angle between 60 and 70 degrees is preferred to reduce the torque. Similarly, a high length-to-thickness ratio of chevrons increases the chevron's bending deformation contribution to the plate's in-plane deformation in the morphing direction. As the bending stiffness of the chevon is much lower than its axial and transverse shear stiffness, a long chevron of between 12.5 and 20 mm is preferred to reduce torque relative to the baseline configuration. Note that the increasing chevron length has a small penalty on fairing distortion; however, the improvement in the torque response is disproportionately large, thereby making it a favourable trade-off.

The parametric study of the fairing variables indicated that adding floating ribs reduced the fairing distortion significantly with a small cost to the torque response. This small increase in torque due to floating ribs can be offset by a small increase in the fairing span. Hence, a design with at least 1 floating rib and a 0.9–1 m fairing span improves both objectives relative to the baseline. Moreover, the study indicated that pre-strain delays the buckling of the top skin, thereby reducing the cross-section distortion. It further extends the linear torque response of the fairing and reduces its torsional stiffness. A pre-strain of at least 10% is required to achieve a 20-degree rotation angle of the pivoted rib (i.e. 40-degree rotation of the wingtip) before the top skin buckles. However, if a lower pre-strain is required to reduce fatigue on the materials, the study showed that 2 floating ribs could eliminate the sharp increase in distortion due to top skin buckling for any pre-strain. Note that the buckling considered here is the panel's global buckling, and the panel's facesheets are likely to buckle locally before the panel buckling, thereby reducing the panel's axial stiffness. Hence, a full-scale FE study is required to study the nonlinearity in the panel's response under large compression.

4. Conclusions

The paper presents a modelling and analysis framework for analysing a morphing fairing for folding wingtip joints made of a flexible sandwich panel with a cellular core. The framework focuses on complexity reduction, firstly, by adopting a two-step modelling approach with homogenisation of the panel properties to equivalent shell properties and modelling of the fairing over the wing section as a shell surface, and secondly, by using a sensitivity study to determine the critical design variables whose effects on the fairing are then analysed in detail using a parametric study. In order to identify the driving features of the panel and the fairing, which contributes to reducing the torsional stiffness of the joint and the cross-section distortion of the fairing, various metrics for quantifying these objectives are studied, and their robustness is evaluated using an initial study varying the number of floating ribs. Torque and displacement metrics were used in the subsequent studies to represent torsional stiffness and cross-section distortion, respectively. A sensitivity study reduced the design

space for the parametric study by selecting only the variables that strongly influence the objectives. The parametric studies for the panel variables show that increasing core thickness contributes significantly to reducing distortion while reducing facesheet thickness and increasing chevron length and chevon angle contributes strongly to reducing torque. In contrast, all fairing variables contribute significantly to both objectives. In particular, increasing pre-strain and span improves both objectives, whereas more floating ribs reduce distortion at the cost of increased torque. Hence, a combined effect of these variables offers an opportunity to reduce the trade-off between the objectives. The study showed the variables that strongly influence the objectives, their trends with the objectives, and their range of values that improve the fairing performance relative to the baseline configuration. The study further highlighted the need to perform a 3-dimensional full-scale re-analysis of the optimal solution, particularly to study the effects of facesheet buckling on the sandwich panel fairing.

Data availability statement

All data that support the findings of this study are included within the article (and any supplementary files).

Acknowledgments

The authors acknowledge the following financial support for the research, authorship, and publication of this article. N M Mahid was supported by the EPSRC Centre for Doctoral Training in Composites Science, Engineering and Manufacturing (Grant Number EP/S021728/1) in the form of funding for his doctoral studies. The work was also supported by Dr Woods's EPSRC Early Career Fellowship AdAPTS (Adaptive Aerostructures for Power and Transportation Sustainability) (EP/T008083/1).

ORCID iDs

Nuhaadh Mohamed Mahid https://orcid.org/0000-0003-1300-7001
Mark Schenk https://orcid.org/0000-0003-0200-2854
Branislav Titurus https://orcid.org/0000-0001-7621-7765
Benjamin King Sutton Woods https://orcid.org/0000-0002-8151-3195

References

[1] International Civil Aviation Organization 2004 *Annex 14—Aerodromes—Volume I—Aerodromes Design and Operations* (available at: https://store.icao.int/en/annex-14-aerodromes)
[2] Federal Aviation Administration 2022 FAA Advisory Circular18150/5300-13B—Airport Design
[3] Boeing *Boeing 777X -Technical Specs* (available at: www.boeing.com/commercial/777x/) (Accessed 27 May 2022)
[4] Castrichini A 2017 *Parametric Assessment of a Folding Wing-Tip Device for Aircraft Loads Alleviation* PhD Thesis University of Bristol
[5] Siddaramaiah V H, Calderon D E, Cooper J E and Wilson T 2014 *Preliminary Studies in the Use of Folding Wing-tips for Loads Alleviation* (Royal Aeronautical Society Applied Aerodynamics Conference)
[6] Wilson T, Kirk J, Hobday J and Castrichini A 2019 Small scale flying demonstration of semi aeroelastic hinged wing tips *19th Int. Forum on Aeroelasticity and Structural Dynamics (IFASD 2019)*
[7] Wilson T, Herring M, Pattinson J, Cooper J, Castrichini A and Rafic A 2019 An aircraft wing with a moveable wing tip device for load alleviation *US Patent App*. 16/067,221
[8] Gu H, Healy F, Jayatilake S, Rezgui D, Lowenberg M, Cooper J, Wilson T and Castrichini A 2024 Flight dynamics of aircraft incorporating the semi-aeroelastic hinge *Aerosp. Sci. Technol.* **147** 109026
[9] Castrichini A, Siddaramaiah V H, Calderon D E, Cooper J E, Wilson T and Lemmens Y 2016 Preliminary investigation of use of flexible folding wing tips for static and dynamic load alleviation *Aeronaut. J.* **121** 73–94
[10] Mahid N M and Woods B K S 2023 Initial exploration of a compliance-based morphing fairing concept for hinged aerodynamic surfaces *Aerosp. Sci. Technol.* **136** 108244
[11] Wilson T, Kirk J, Hobday J and Castrichini A 2022 Update on AlbatrossONE semi aeroelastic hinge small scale flying demonstrator project *Int. Forum on Aeroelasticity and Structural Dynamics* (*Madrid, Spain*)
[12] Thill C, Etches J A, Bond I P, Potter K D and Weaver P M 2010 Composite corrugated structures for morphing wing skin applications *Smart Mater. Struct.* **19** 124009
[13] Ursache N M, Melin T, Isikveren A T and Friswell M I 2008 Technology integration for active poly-morphing winglets development *ASME 2008 Conf. on Smart Materials, Adaptive Structures and Intelligent Systems* (*Ellicott City, Maryland, USA, 28–30 October 2008*) (https://doi.org/10.1115/SMASIS2008-496)
[14] Bubert E A, Woods B K S, Lee K, Kothera C S and Wereley N M 2010 Design and fabrication of a passive 1D morphing aircraft skin *J. Intell. Mater. Syst. Struct.* **21** 1699–717
[15] Vocke R D, Kothera C S, Woods B K S and Wereley N M 2011 Development and testing of a span-extending morphing wing *J. Intell. Mater. Syst. Struct.* **22** 879–90
[16] Kothera C S, Woods B K, Wereley N M, Chen P C and Bubert E A 2011 Cellular support structures used for controlled actuation of fluid contact surfaces *U.S. Patent No* 7,931,240
[17] Olympio K R and Gandhi F 2009 Zero Poisson's ratio cellular honeycombs for flex skins undergoing one-dimensional morphing *J. Intell. Mater. Syst. Struct.* **21** 1737–53
[18] Heeb R M, Dicker M and Woods B K S 2022 Manufacturing and characterisation of 3D printed thermoplastic morphing skins *Smart Mater. Struct.* **31** 085007
[19] Woods B K S and Heeb R M 2023 Design principles for geometrically anisotropic thermoplastic rubber morphing aircraft skins *J. Intell. Mater. Syst. Struct.* **34** 29–46
[20] Mahid N M, Schenk M, Titurus B and Woods B K S 2023 Parametric studies of flexible sandwich panels as a compliant fairing for folding wingtip joints *ASME 2023 Conf. on Smart Materials, Adaptive Structures and Intelligent Systems. SMASIS2023* (American Society of Mechanical Engineers)
[21] Gigliotti L and Pinho S T 2015 Exploiting symmetries in solid-to-shell homogenization, with application to periodic pin-reinforced sandwich structures *Compos. Struct.* **132** 995–1005
[22] Hii A K W and Said B E 2022 A kinematically consistent second-order computational homogenisation framework for

thick shell models *Comput. Methods Appl. Mech. Eng.* **398** 115136
[23] Heeb R M, Dicker M and Woods B K S 2022 Design space exploration and modelling of GATOR 3D printed morphing skins *ASME 2022 Conf. on Smart Materials, Adaptive Structures and Intelligent Systems. SMASIS2022* (American Society of Mechanical Engineers)
[24] NinjaTek 2016 NinjaFlex 3D Printing Filament. *Fenner Precision Polymers* (available at: https://ninjatek.com/wp-content/uploads/NinjaFlex-TDS.pdf)
[25] NinjaTek 2016 Armadillo 3D Printing Filament. *Fenner Precision Polymers* (available at: https://ninjatek.com/wp-content/uploads/Armadillo-TDS.pdf)
[26] AIRBUS 2020 A320 Aircraft Characteristics—Airport and Maintenance Planning *AIRBUS S.A.S., Customer Services, Technical Data Support and Services* (Blagnac Cedex) p 31707
[27] Dassault Systemes Simulia Corp 2018 Abaqus Documentation *SIMULIA User Assistance 2018. Dassault Systemes Simulia Corp*
[28] Ameen M M, Peerlings R H J and Geers M G D 2018 A quantitative assessment of the scale separation limits of classical and higher-order asymptotic homogenization *Eur. J. Mech. A/Solids* **71** 89–100
[29] Gibson L J and Ashby M F 1997 *Cellular Solids: Structure and Properties* (Cambridge University Press)
[30] Huang J, Gong X, Zhang Q, Scarpa F, Liu Y and Leng J 2016 In-plane mechanics of a novel zero Poisson's ratio honeycomb core *Composites* B **89** 67–76
[31] Coenen E W C, Kouznetsova V G and Geers M G D 2010 Computational homogenization for heterogeneous thin sheets *Int. J. Numer. Methods Eng.* **83** 1180–205
[32] Gruttmann F and Wagner W 2024 A FE2 shell model with periodic boundary conditions for thin and thick shells *Int. J. Numer. Methods Eng.* **125** e7433
[33] Ladson C L, Brooks J and Cuyler W 1975 *Development of a Computer Program to Obtain Ordinates for NACA 4-digit, 4-digit Modified, 5-digit, and 16 Series Airfoils* (NASA Langley Research Center)
[34] Chen D H 2011 Equivalent flexural and torsional rigidity of hexagonal honeycomb *Compos. Struct.* **93** 1910–7
[35] Huang J, Zhang Q, Scarpa F, Liu Y and Leng J 2016 Bending and benchmark of zero Poisson's ratio cellular structures *Compos. Struct.* **152** 729–36
[36] Timoshenko S and Goodier J N 1970 *Theory of Elasticity* 3rd edn (McGraw-Hill)
[37] Chen D H 2011 Bending deformation of honeycomb consisting of regular hexagonal cells *Compos. Struct.* **93** 736–46
[38] Reissner E and Stein M 1951 Torsion and transverse bending of cantilever plates *NACA-TN-2369* (NASA) (available at: https://ntrs.nasa.gov/citations/19930090894)